Biomedical Signal Processing and Control 71 (2022) 103230

Contents lists available at ScienceDirect

Biomedical Signal Processing and Control

journal homepage: www.elsevier.com/locate/bspc

Deep Learning based Vertebral Body Segmentation with Extraction of Spinal Measurements and Disorder Disease Classification

Rao Farhat Masood [a,*], Imtiaz Ahmad Taj [a], Muhammad Babar Khan [b], Muhammad Asad Qureshi [c], Taimur Hassan [d]

[a] Department of Electrical Engineering, Capital University of Science and Technology (CUST), Islamabad, Pakistan
[b] Department of Radiology, Combined Military Hospital, Rawalpindi, Pakistan
[c] Department of Spinal Surgery, Combined Military Hospital, Rawalpindi, Pakistan
[d] Center for Cyber-Physical Systems, Khalifa University of Science and Technology, Abu Dhabi, United Arab Emirates

ARTICLE INFO

Keywords:
Lumbar spine dataset
Spinal measurements
Automated disease classification

ABSTRACT

Assessment of medical images and diagnostic decision making of lumbar associated diseases by clinicians is invariably subjective, time consuming and challenging task. Presently, clinicians make use of either manual or semi-automated computer-aided tools to make relevant measurements for adding vote of confidence to their grading and evaluation. Lacking reliability and offering substantive dissimilarity once performed by different clinicians, these methods complicate the evaluation process. In an effort to support the decision making process of clinicians, in this paper we present a lumbar assessment framework with autonomous extraction of spinal measurements. Furthermore, an effort is made to address the challenges faced by clinicians while assessing disorders including spondylolisthesis and assessment of lumbar lordosis (LL) by proposing novel disease classification methodologies. For spondylolisthesis classification, we achieved an accuracy of 89% by using angular deviation metric whereas, 93% accuracy for determining adequacy/inadequacy in LL assessment through computation of area within enclosed lumbar curve region. Our framework involves semantic segmentation of vertebral bodies (VBs) using ResNet-UNet where we achieved DSC of 0.97 and IoU of 0.86. Subsequently, we achieved a statistically significant correlation coefficient R and encouraging mean absolute error (MAE) with clinicians' grading for measurements involving lumbar lordotic angle (LLA), lumbosacral angle (LSA), VB dimensions and lumbar height. In addition to this, we have publicly released the dataset with all the clinicians markings at https://data.mendeley.com/datasets/k3b363f3vz/2.

1. Introduction

Chronic backache in general and lower back pain in particular is considered one of the most commonly naturally occurring ailment by both the radiologists and spinal surgeon community [22,102,93]. Lumbar spine or lower-back is the area which once effected gives rise to lower-back pain clinically termed as lumbago. In most of the cases, lumbago is associated to muscular or ligaments strain which is mostly caused by improper weightlifting and sitting in improper posture for a longer duration [16]. In other cases, lumbago can also be caused by nerve compression, which as a result radiates pain in either or both of the legs, commonly referred as sciatica [108]. Nerve compression can also be caused by fracture of the vertebral body (VB) or vertebral arch (VA) bone thereby reducing the space between the vertebral bodies, causing the intervertebral discs (IVD) to slip or herniate [100]. As a consequence, the protruding or slipped discs exert pressure on the existing nerves causing tingling pain in legs and lower body paralysis in case of nerve damages [115]. The patient undergoes a suitable surgical intervention procedure, including, but not limited to, decompression, in order to relief the nerves of pressure, thereby enhancing the quality of life (QoL) [44].

Diagnosing lower back pain is itself a challenging and laborious task where the imaging including X-ray and MRI scan of patient provides the referring clinician with precise information regarding the spinal ailment and enabling the clinician in establishing correlation between the images and the pain symptoms[16,91]. At present, the spinal surgeons and radiologist community are dependent on completely manual or semi-automated methods i.e., computer assisted software-based image

* Corresponding author.
E-mail address: farhatmasood.fm@gmail.com (R.F. Masood).

https://doi.org/10.1016/j.bspc.2021.103230
Received 30 March 2021; Received in revised form 31 August 2021; Accepted 30 September 2021
Available online 12 October 2021
1746-8094/

understanding methods for diagnosis purposes, which are certainly laborious and time-consuming methods. The analysis report generated by radiologists is focused on identification and presence of spinal disease whereas the spinal surgeon clinically evaluates the patients with reference to the exhibited symptoms. Equally important is the assessment of spinal alignment, spinal deformation and spinal balance as it has been clinically established that lumbar load bearing and impact of stress sharing are remarkably affected in altered LL i.e., the inward angle of lumbar spine [41].

Researchers, over a period of time have developed association with altered spinal alignment with lumbago [12,26], and have emphasized on its restoration for adequate spinal balance [15,45,59]. Identification of these measurements is an extremely important pre-operative procedure to restore the normal lordosis enabling posture correction and spinal balance restoration. The relevant spinal measurements enable the spinal surgeon in making an estimation of effective posture correction post-operative procedure.

In order to make this research work clinically relevant, the desired outcome was to offer an autonomous spinal assessment toolkit to clinicians enabling them in mass screening the images and adding vote of confidence to their traditional assessment methodology. In pursuit of the outcome, following are the key objectives:

- Introduction of an annotated lumbar spine MRI dataset in sagittal plane with relevant spinal measurements, thereby, giving the research community a composite dataset for both qualitative and quantitative ability to assess the lumbar spine. Presently, to best of our knowledge, composite dataset encompassing annotated images and spinal measurements is not shared for research collaboration.
- Offering an accurate, consistent and robust solution for performing semantic segmentation task. In this aspect, we have crafted a customized conventional algorithm for performing segmentation task and compared its performance with deep learning models.
- Acquisition of automated spinal measurements, where we have covered both distance based and angular measurements.
- Identification of presence of spinal disorders including spondylolisthesis and lumbar lordosis i.e., curvature of lumbar spine. Here, we have presented novel methods to assess the spinal disorders.

The paper is organized into 9 sections where Section 2 covers the clinicians perspective of assessment of lumbar spine. Section 3 sequentially unfolds the related work encompassing datasets3.1, segmentation methods3.2 and spinal measurements3.3 as discussed in Section 2. After reviewing the related work research gap is identified in Section 4 followed by the major contributions in this paper. Section 5 covers the details of development of dataset which is used in this research. The autonomous VB extraction and spinal measurement framework as graphically showcased in Fig. 7 is explained in details in the subsequent sections. Section 6 is about the traditional machine learning based segmentation algorithm and segmentation performed using deep learning methods. In Section 7, we describe the details about the automated spinal measurements, whereas, Section 8, covers our proposed methodologies to classify spinal disorders including spondylolisthesis and assessment of LL. Section 9 presents the evaluation results (category wise), where we evaluate results of semantic segmentation as well as perform cross-verification of our proposed automated toolkit for acquisition of spinal measurements with the clinician's markings. Finally, we conclude our work and findings and shed light on future directions.

2. Clinical evaluation of lumbar spine disorders

As already well established by the clinicians that MRI images offer superior image quality once compared to X-ray images [4,5,71]. Here, we present summarized overview of clinicians including radiologists' and spinal surgeons evaluation of the lumbar spine.

2.1. Radiologists' viewpoint

- The role of imaging is to localise and quantify the disease process and its effects on normal anatomy. This helps the spinal surgeons in planning appropriate intervention [21].
- While making analysis of the lumbar spine the presence of degenerative intervertebral disc diseases and related VB deformations are noted [28,94].
- Lumbar spine is graded as the most susceptible region to degenerative changes of the spine owing to impact of body weight [93,36,62] particularly involving the intervertebral discs levels L3-L4, L4-L5 and L5-S1 [58].
- The spinal curvature is analysed in mid sagittal plane. Normally the lumbar spine has an anterior curvature ranging from 20–80 degrees [83] owing to the viscoelastic properties of the functional spine unit. In case this lordotic curve exceeds and the lordotic angle becomes large the term is called 'Sway Back' or hyper-lordosis. The converse is called 'Flat Back' or hypo-lordosis [31]. This malalignment has been implicated in causing backache due to abnormal weight on the lumbar spine and consequent degradation of the viscoelastic properties of the support structures of the spine [77,72,69].

2.2. Spinal surgeons' viewpoint

- A spinal surgeon clinically examines the candidate subject and correlates the clinical findings with the imaging and the radiologist report [84].
- Then based on the severity of abnormal spine pathology, further physical examination of the subject is conducted [127].
- Afterwards, if required, detailed evaluation of spinal alignment and spinal balance is performed through manual spinal analysis from X-ray and MRI scans including lordotic angle (LLA), lumbosacral angle (LSA), pelvic incidence angle (PIA), lumbar spine height (LSH), IVDs size both at posterior and anterior sides[57].
- Depending on the severity of spinal disease/disorder, pain threshold and inclination of the candidate subject, a suitable decision modality is adopted for specific surgical intervention procedure[45,57].
- In other cases, where surgical intervention is avoided certain conservative treatments with specific physical exercises may also be recommended [97,91].
- The surgical intervention procedures related to lumbar spine can be grouped into two major categories, namely fusion and decompression [29,34,90]. The *fusion* procedure, in which VBs are fused or joined together to limit movement between them, is graded more invasive and surgically intensive as compared to decompression procedure [39,66,99]. In *decompression*, the part of IVD or bone compressing the exiting nerve roots is removed, thereby relieving the pressure [79,94].

In subSections 2.2.1 and 2.2.2 brief overview of spinal disorders including spondylolisthesis and assessment of lumbar lordosis from clinicians' perspective are presented which would enable to reader to develop better understanding while reading Section 8. Additionally, in subSection 2.2.3, clinically relevant spinal measurements are overviewed for subsequent proposal of method for automated extraction of these measurements as covered in Section 7.

2.2.1. Assessment of spondylolisthesis

Spondylolisthesis is a common term for the misalignment of a VB posteriorly or anteriorly due to bone stress fracture clinically termed as spondylolysis[105]. While performing grading of spondylolisthesis, the clinicians follow Meyerding classification [80] from grade I to grade V at an equal interval of 25 % as graphically depicted in Fig. 1. The *limitation* of Meyerding classification is qualitative assessment of spondylolisthesis which is prone to variation based on the experience level of clinician[7]. Furthermore, this method is dependent on the structure of the VB end-

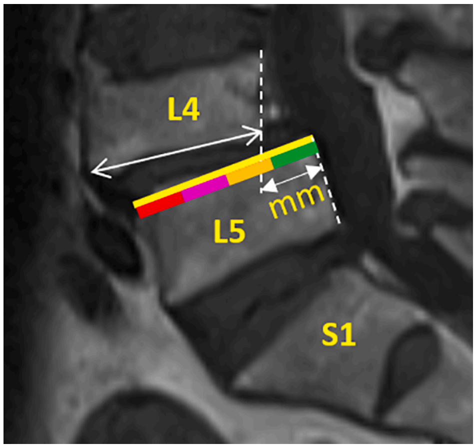

Fig. 1. Assessment of Spondylolisthesis using Meyerding Classification.

plates which once compromised due to osteophyte formation will drastically cause variation in the assessment [32,7]. In an effort to overcome this limitation, we have proposed an automated method for assessment of spondylolisthesis which is covered in Section 8.1.

2.2.2. Lumbar lordosis (LL) assessment

Before surgical intervention, the surgeon manually performs certain measurements for developing better understanding of shape and structure of vertebral column in order to select the most suitable procedure. The typical methods include use of computer assisted software, physically measuring dimensions on patient by using flexible rulers [87], inclinometers [70] or spinal mouse [103]. Despite being most significant spine parameter [113], the assessment of spinal curvature is lacking quantitative evaluation as the readings are prone to variation due to observers' manual or semi-automated handling [124]. Typically, a standing X-ray radiograph is performed for evaluation of lordotic curve followed by manual angular measurements which includes Cobb angle [56] i.e., Modified Cobb Method [125], which has become a standard for evaluating lordotic curve [42] in the sagittal plane [123]. As shown in Fig. 2, θ is the angle of intersection between the perpendicular lines drawn from superior end-plate of L1 and superior end-plate of S1.

The basic *limitation* of using Cobb method, as reported in a research [92], is the reliance on end-plate structure to measure the angle. It is also seen that owing to osteophyte formation, the end-plate structure is compromised and resultantly the Cobb method is prone to variation during inter-observer assessment [35]. In order to overcome this limitation, various other techniques were introduced by medical practitioners. The spinal surgeon may adopt other measurement methods to make numerical analysis. A summary of some of the techniques is presented in below:

- **Ishihara Index**
  A straight line is formed joining posterior-inferior corner of L1 and L5 VBs, while remaining in between VBs inferior corner points are connected perpendicularly. The ratio of sum of lengths of perpendicular lines to the spinal length (L1-L5) is the measure of Ishihara index [53]. The same is represented by $I = \sum d_i/L$ where, L is the lumbar length as depicted by magenta dotted line in Fig. 3 (a) whereas, $\sum d_i$ is the sum of red line segments.
- **Voutsinas and MacEwen (VM) Method**
  The researchers used anterior corner-points and selected maximum orthogonal distance from corner-points to the straight vertebral line as opposed to posterior corner points and sum of perpendicular distances. The same is reflected in the expression $I = d/L$, where, d is maximum perpendicular distance shown in red in Fig. 3 (b) to the lumbar height shown in magenta [122].
- **Tangential Radiologic Assessment of Lumbar Lordosis (TRALL)**
  Angle of intersection θ as shown in Fig. 3 (c) between the lines formed by joining L1 and L5 VBs to maximum posterior distanced corner-point from the magenta spinal line is the TRALL metric [113].
- **Harrison Posterior Tangent Method (HPTM)**
  The angle of intersection θ between the tangent lines made by connecting posterior-inferior and posterior-superior corner-points of two superior VBs and posterior-inferior and posterior-superior corner-points of two inferior VBs as depicted in the Fig. 3 (d), [40,42,41].
- **Centroid Method**
  The method uses centroids [23] instead of corner-points for computation of angle of intersection θ as shown in Fig. 3 (e).
- **Area Under the Curve (AUC) Method**Yang et al. proposed AUC method in which a curve is plotted connecting the posterior corners of lumbar VBs. Afterwards, superior corner-point is connected directly to the inferior VB corner point [126]. The same is showcased in Fig. 3 (f).

The alternate assessment methods including Chen and Yang methods 2.2.2, involve multiple measurements, where the Chen [23] centroid method shown in Fig. 3 (e) was found to be most calculation intensive hence more reliable [123,104] and Yang method [126] was implemented through software-assistance as shown in Fig. 3 (f). The reliability

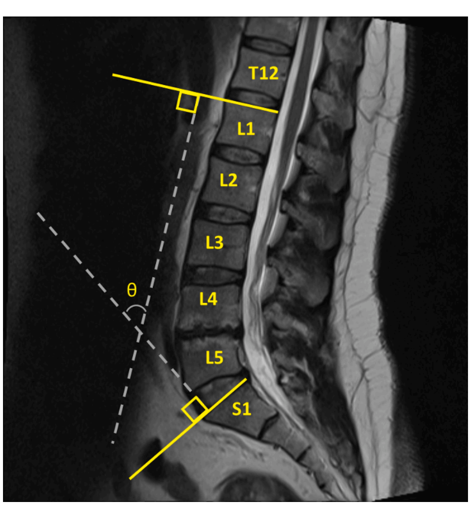

Fig. 2. Modified Cobb Angle θ Measurement Method.

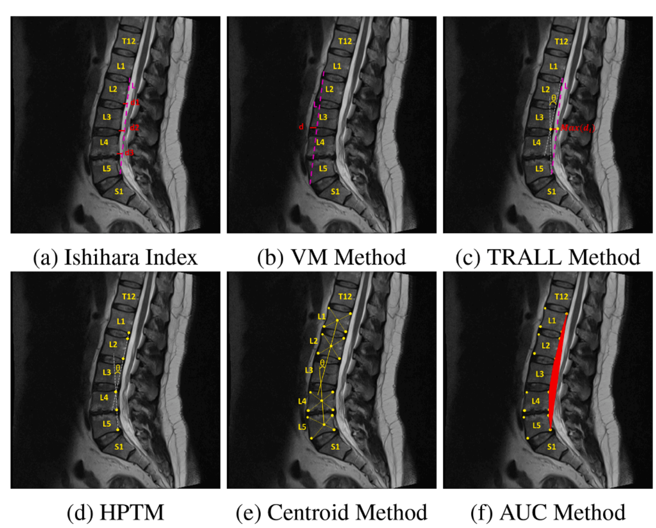

Fig. 3. Methods used for Assessment of Lumbar Lordotic Curve.

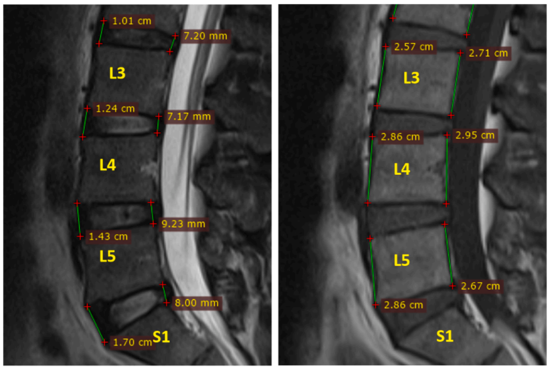

(a) IVB Distance(s) (b) VB Dimension(s)

Fig. 4. IVB Distances and VB Sidewalls Dimensions.

and reproducibility of these alternate methods was found to be superior than commonly used modified Cobb method [86,41]. In this paper, we augment Chen and Yang methods as presented in 9.3.2 and correlate the accuracy of our method with clinicians' measurements using Cobb method.

2.2.3. *Vertebral body dimensions and related measurements*

Additionally, some other important measurements related to VBs dimensions including the VB side walls, VB endplates and IVB distances at both anterior and posterior sides are also performed. Angular measurements are also performed. These measurements give information about the VB fracture, reduction in space and size of IVD or VB thus enabling the clinician in establishing correlation between the symptoms and clinical findings[124]. The space between adjacent VBs is shown in Fig. 4 (a), whereas the sidewall dimensions is shown in Fig. 4 (b). Any abnormality in this general trend is also noted thereby making an indication for spinal misalignment or imbalance.

Thus, in contrast with radiologists' opinion, a spinal surgeon relies on detailed in-depth measurements, as covered in sub-Section 2.2.3, in order to ascertain presence or absence of surgical site and severity of spinal disorder for selection of the most appropriate surgical procedure or recommendation of conservative treatment. Maximum reliance is on these quantitative measurements before making suitable decision for spinal intervention, enabling the surgeon to establish a correlation in order to determine the efficacy of the surgical procedure in posture correction and restoration of spinal balance.

3. Related work

Many researchers have worked on measuring lumbar spine disorders using MRI scans. Here, many of the existing approaches utilize publicly available datasets [112], while some of them have also been extensively tested on locally acquired clinical data [75]. In addition to this, many of the existing literature highlighted the significance of MRI scans for objectively measuring spinal misalignments [123]. Also, many clinicians have presented studies in which they highlighted the significance of mid-sagittal MRI scans for objectively measuring the degree of misalignments as per the clinical standards[43]. In order to best present the literature, we have categorized them into three sub-section where, at first, we present the literature showcasing some of the public datasets (3.1) which have been recently introduced to evaluate the performance of the semi-automated, and fully automated frameworks. In the second, sub-section we present the methods and techniques used to perform segmentation (3.2) tasks including both traditional (3.2.1) methods and deep learning methods (3.2.2). Lastly, we present some of the frameworks which have been proposed for measuring spinal disorders(3.3).

3.1. *Publicly available lumbar spine datasets*

Over the past decade, many researchers have publicly released high-resolution and well-annotated datasets for accessing lumbar spine disorders. Here, the contributions of H. Bennani et al. are appreciable who made use of 3D modelling through the use of Agisoft Photoscan software, which is currently upgraded to Agisoft Metashape [2], to acquire complete 360° representations of lumbar spine [14]. Another free resource available online for providing public access is provided by Imperial College, London which comprised of computed tomography (CT) Scan images of 125 patients [37]. Multiple resources of labelled lumbar spine database are available on SpineWeb [112], however, the datasets are mostly composed of CT images and the ones with MR images are limited to less than 100 scans. In another work, Burian et al. have also released the ground truth images, in sagittal views, within their dataset highlighting the VBs from L1 and L5 while excluding the sacrum bone. Their dataset comprises of 54 images of healthy Caucasian subjects including water, fat and proton density fat fraction (PDFF) images and relevant masks, however, no information regarding the ailment related to spinal disorder was given in the dataset [18]. In a recent work, Löffler et al. [65] provides vertebral segmentation masks for spine images with annotations comprising of fractures or spinal abnormalities. The dataset composed of CT scans of 141 patients is publicly available online [88]. The MRI database that we have used is publicly available at Mendeley Website [114], providing ample variability with total of 515 scans of subjects with symptomatic back pains. On the same dataset, Natalia et al. [85] have manually labelled the axial views of last three-disc levels. Later on, with the supervision from the ground truth labels, Al-Kafri et al. [3] performed detection of spinal stenosis commonly termed as narrowing of nerve canal, using deep learning based on U-Net [98] architecture.

3.2. *Segmentation methods*

In this sub-section, the previous work done to perform medical image segmentation is highlighted in two sub-parts. In the first sub-part 3.2.1, techniques based on conventional methods is presented, while in the second sub-part 3.2.1 methods involving use of deep learning to perform segmentation tasks is covered.

3.2.1. *Conventional methods for medical image segmentation*

Many researchers have implemented a plethora of techniques and methods to perform segmentation over a period of time. In this paper, we have reviewed some of the methods, including use of Active Shape

Model (ASM) [110], universal shape model [6], normalized cuts [20], template matching using Generalized Hough Transform (GHT) [51,78], application of Gabor filter bank [134] and random forests [38]. The use of k-mean clustering was also advocated by the researchers to perform the clustering based segmentation task [11,60,78].

3.2.2. Medical image segmentation by deep learning methods

Here, we present the related segmentation work performed using deep learning architectures. Suzani et al. [116] achieved 96 and 94.4 percent accuracy and precision respectively by 6 layered deep forward network. Lu et al. [68] performed the segmentation task on sagittal MR images by making use of U-Net architecture, that is a deep neural network architecture, achieving an accuracy of 94 % and dice similarity coefficient (DSC) score of 0.93 with standard deviation of 0.02. In another work, the researchers have performed the segmentation task on 15 CT scans using Fully Connected Network (FCN) and obtained DSC 0.9577 $\pm$ 0.81, Jaccard Co-efficient (JC) 0.9190 $\pm$ 1.48 and average symmetric surface distance (ASSD) of 0.37 $\pm$ 0.06 mm [54]. Lessmann et al. [61] made use of CNN for vertebrae segmentation and achieved an accuracy of 97 % and DSC of 94.9 %. Rak et al. [96] achieved a DSC score of 0.938 using UNet on whole spine MR images. Huang et al. [52] achieved a superior IoU score for vertebra segmentation with UNet architecture on a dataset of 100 MRI in which 50/50 split was used for training and testing purpose. Tang et al. [118] used Dual Densely Connected U-Net (DDUNet) architecture to segment out the regions on axial scans extracted from CT Images. The metrics pixel accuracy (PA) – 0.9913, mean pixel accuracy – 0.9099, mean Intersection over Union (IoU) 0.8331 and frequency weighted IoU 0.9835 were evaluated. In an another work [48], RAGNet [47], proposed by the same group is used for performing retinal lesions segmentation. In their work, they have compared the performance of various deep learning frameworks on lesion segmentation. They exhibited that RAGNet shows most promising results as compared to other models like U-Net [98], SegNet [9] and PSPNet [132]. Harvesting the potential of the pre-trained networks to perform segmentation tasks, in this paper we trained various models through fine-tuning mode of transfer learning, details of which are covered in Section 6.2.

3.3. Spinal measurements

In this section, we shed light on some of the recently introduced semi-automated and fully automated frameworks for the screening of spinal disorders. We also want to highlight here that, due to the scope of the proposed study, we are primarily not focusing on the manual methods which are used by the spinal surgeons for screening the spinal disorders, mainly due to the fact that these manual methods involve physical examination of the subject.

3.3.1. Semi-automatic methods

The use of Digital Imaging and Communication in Medicine (DICOM) [27] viewers with built-in measurement tools have been extensively used by the researchers and clinicians over the past and are still in use of both spinal surgeons and radiologists while carrying out spinal measurements. Furthermore, the spinal curvature measurements through these computer-aided software mostly rely on manual vertebral markings [33,95,33,101,121]. In another work, Babai et al. [8] made use of AutoCAD software to measure the LL angle using 30 standing X-ray images. The work of MacIntyre et al. [71] compared the spine curve estimation by making use of IONMed Mobile phone application with the measurements made by digital inclinometers. Zhang et al. [129] measured Cobb angle for scoliosis cases using 105 radiograph images in coronal plane and found 0.98 correlation between the manual i.e., clinicians markings and computer aided measurement with the mean absolute error of $< 3^{\circ}$.

All the above narrated examples fall in the category of computer assisted measurements where a software helps to establish a relationship between the geometrical structure which involves manual identification and selection of landmarks for measurements.

3.3.2. Fully automated methods

More recently, researchers have developed machine learning and deep learning screening frameworks thereby supporting the clinicians' manual diagnosis. Here, Pang et al. [89] achieved the mean absolute error (MAE) of 1.23 mm while computing spinal distances including VB dimensions from L1 superior-left corner to L5 inferior-left corner within 225 scans. Their method, however, involves manual user input for identification of superior-left corner of L1 VB and inferior-left corner of L5 VB for providing reference to ROI cropping. Similarly, Masad et al. [73] have also measured LL in 32 T2-MR sagittal images and established a correlation of 0.932 with manual Cobb Angle measurement. Moreover, Cho et al. [24] presented the use of U-Net architecture and performed segmentation of lumbar spine on 151 X-ray scans. Subsequently, they computed the lordotic angle where they achieved the MAE of 8.055°.

4. Gap analysis and contributions

After going through the literature, we found that, to the best of our knowledge, there is currently no publicly available lumbar spine dataset which provides an extensive set of clinically significant spinal measurements, which is extremely useful for developing the robust frameworks for the autonomous screening and grading of lumbar spine disorders. These spinal measurements are clinically significant [34], as they can aid the spinal surgeons in understanding the underlying spinal pathology (of the candidate subject) before beginning the surgical procedure [39]. Therefore, the automated spinal measurement toolkit being presented in this study will not only reduce the clinician's time by mass screening normal cases, but it can also facilitate their recommendation by providing clinically significant quantitative measures. Thus, the main contribution of this paper are four-folds, as described below:

1. To the best of our knowledge, this paper presents first publicly released composite dataset[1] from expert radiologists and spinal surgeons on publicly available lumbar spine MRI scan dataset provided by Sudirman et al. [114]. The existing MRI dataset is suitable for IVDs analysis as the annotations are done in axial plane. Our labelled image dataset in sagittal plane comprises of images, ground truth labels and relevant spinal measurements offering the researchers with a quantitative ability while observing the spinal misalignments.
2. We also provide evidence advocating the superiority of deep learning architecture over conventional/traditional machine learning methods for image segmentation.
3. Furthermore, we present a fully automated approach towards accessing clinically significant spinal measurements within the lumbar spine area, which can aid the clinicians in quantitatively

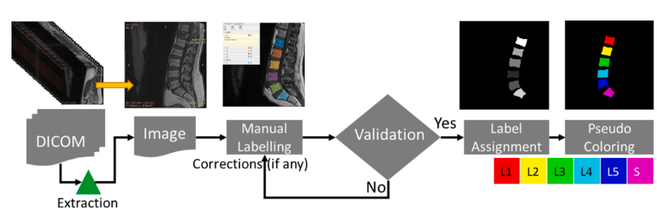

Fig. 5. Process Flowchart (Image Extraction, Labelling and Validation).

[1] The composite dataset with relevant spinal measurements is publicly released for the research community at https://data.mendeley.com/datasets/k3b363f3vz/2.

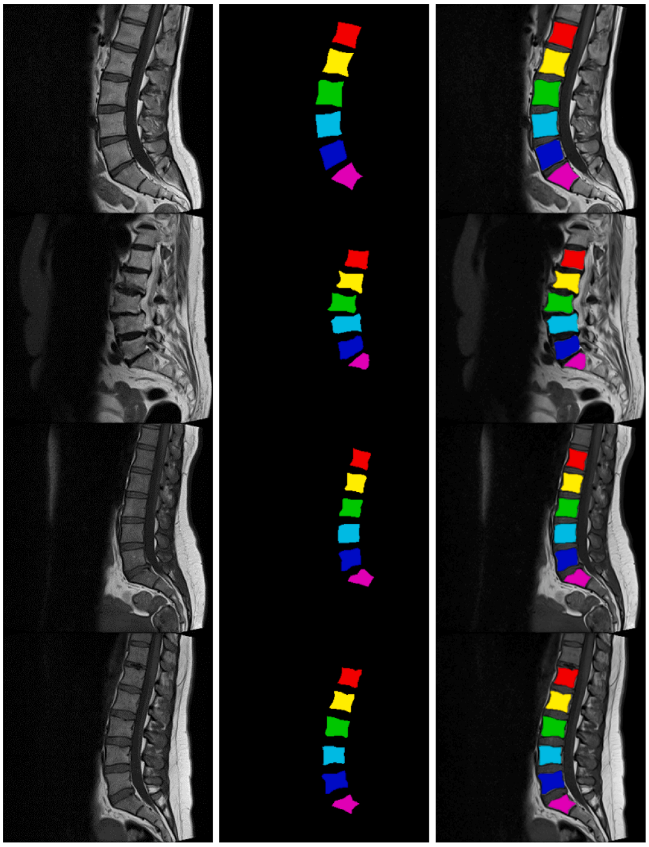

(a) Original Image(s) (b) Labelled Image(s) (c) Overlay Image(s)

Fig. 6. Result of Image Annotation.

Algorithm 1: VBSeg – Vertebral Body Segmentation

Input: Original Image I
Output: Extracted Image I_{VB}
$I_c \leftarrow$ ContrastAdjustment(I)
$I_h \leftarrow$ CLAHE(I_c)
$I_s \leftarrow$ UnsharpMasking(I_h)
$I_b \leftarrow$ Binarization(I_s)
$I_b^f \leftarrow$ ImageFill(I_b)
$I_b^{f,a} \leftarrow$ AreaOpening(I_b^f)[RejectArea = $Area < \tau$]
$I_b^{f,a,o} \leftarrow$ ImageOpening($I_b^{f,a}$)[*5x5, Diamond Structure Element*]
$I_b^{f,a,o,s} \leftarrow$ Smoothing($I_b^{f,a,o}$)[*Anisotropic*]
$I_{VB}^{pv} \leftarrow$ ShapeFilter($I_b^{f,a,o,s}$)[$\rho \leftarrow$ *Extent, Area, MA/mA*]
for $I_{VB}^{pv} \neq I_{VB}^{v}$ **do**
  $nVB \leftarrow$ CountVB(I_{VB}^{pv})
  if $nVB = valid$ **then**
    $I_{VB}^{v} \leftarrow (I_{VB}^{pv})$
  else
    if $nVB = invalid$ **then**
      ShapeFilter($I_{bw}^{f,a,o,s}$)[$\rho \uparrow$ if $nVB < valid$, $\rho \downarrow$ if $nVB > valid$]
    end
  end
end
$I_{VB} \leftarrow I_{VB}^{v}$

observing the spinal misalignments. The detailed investigation of radiologists' analysis of MR scan vis-á-vis a spinal surgeons' preference enabled us to establish clinical relevance towards building an automated spinal measurements scheme.

4. Lastly, we present an automated spinal deformation classification methodologies for spondylolisthesis, hyper/hypo/normal LL assessment.

5. Development of ground truth images for mid-sagittal views lumbar spine MRI scans

In this section, the details about the annotations marking principles (and protocols) are covered. To mark the mid-sagittal view lumbar spine MRI scans [114] at pixel-level for vertebral column extraction, we have used MATLAB R2020a Image Labeler Application [74]. Moreover, we used the RadiAnt DICOM Viewer by Medixant [76] to visualize 2D slices (within the 3D volumetric MRI data). Here, we also want to mention that out of 515 MR images, we annotated 514 scans and dropped only one scan because it was found unsuitable for the evaluation purposes in sagittal view. The amount of time consumed in label assignment is around 12 to 15 min (on average), whereas another 5 to 7 min were consumed on validation and necessary correction. In total, there are three steps which were involved in the ground truth labeling as shown in Fig. 5. Moreover, the resultant ground truth images are presented in Fig. 6.

5.1. Image extraction

As mentioned above, the DICOM images are read using the RadiAnt DICOM Viewer by Medixant. The mid-sagittal slices are highlighted by the expert radiologist in order to create the ground truth image. The identified slices are exported and are stored in a separate folder. Since, the bone presents the same contrast in both T1 and T2 images [64], therefore, through empirical evaluation, we found the selection of either T1 or T2 images, suitable for spinal measurements. While extracting the

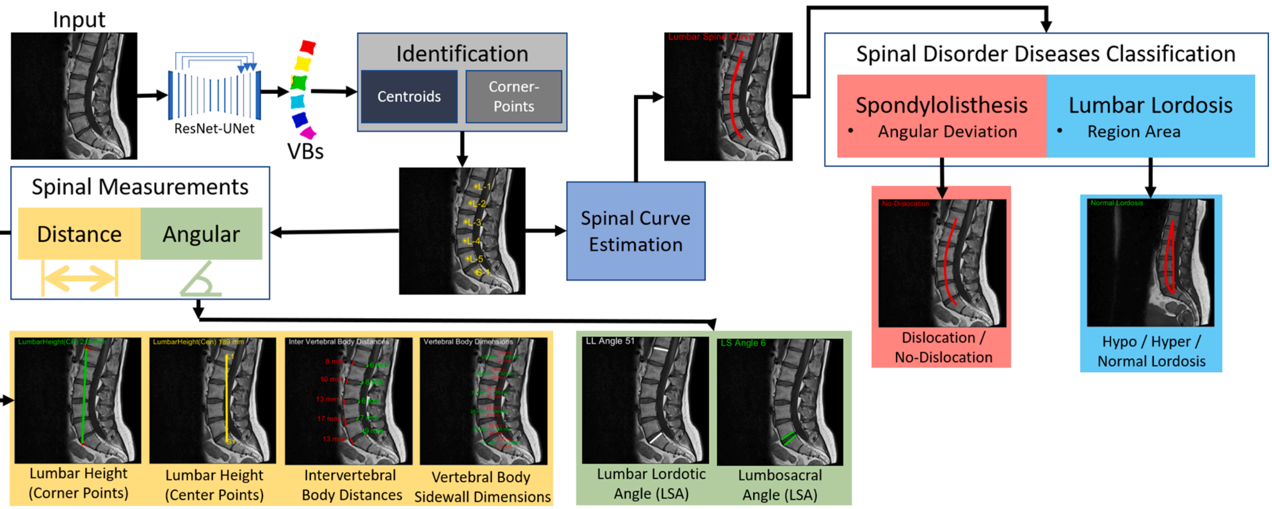

Fig. 7. Block Diagram.

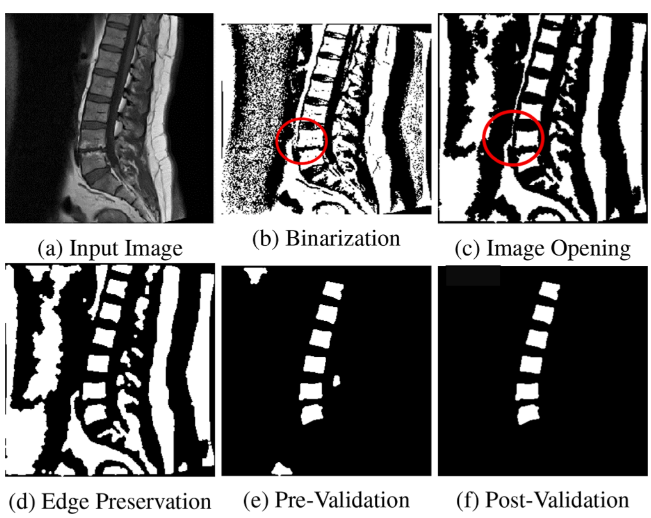

Fig. 8. Selected Images Results of VBSeg Algorithm.

image slices, relevant pixel spacing information is also stored to be used in subsequent part while performing conversion in measurements from number of pixels to millimeters.

5.2. Image annotation

The extracted images are then loaded in image labeler application. Here, our objective is to facilitate the semantic segmentation of VBs. Therefore, we marked (pixel-wise) the six labels, namely, L1, L2, L3, L4, L5, S as shown in Fig. 5. Moreover, the region around the vertebral body is plotted using smart polygon/ polygon tool (whichever gave the most fill). Afterward, fine-tuning is performed using the brush tool to fill the desired regions which were missed by polygon/smart-polygon tool.

5.3. Validation

The final validation and evaluation of correctness of labelled images are ascertained by expert spinal surgeons. Any incorrectness observed by the spinal surgeon is rectified. The results of annotation is displayed as Fig. 6, where a sample of result is showcased.

6. VB segmentation

In this section, a performance comparison is made between traditional machine learning methods and deep learning networks for semantic segmentation. In the first sub-Section 6.1, we present our customized algorithm (we call it VBSeg) being completely autonomous, without involving user intervention. Later, in the second sub-Section 6.2, deep learning methods used to perform the segmentation task are presented.

6.1. Traditional method

In our tailored custom algorithm (VBSeg), the first stage comprises of pre-processing stage in which input image (I) as shown in Fig. 8 (a) is adjusted for contrast (I_c) [135] and histogram equalization (I_h) [107] is performed. Later, the details are sharpened (I_s) using unsharp masking. Binary image (I_b) is acquired through applying adaptive binarization [17]. The final binary mask is obtained by performing image hole filling (I_b^f) to fill the disjoint areas within a region and area opening ($I_b^{f,a}$) to remove the small objects not commensurate ($Area< \tau$) to the VBs. The

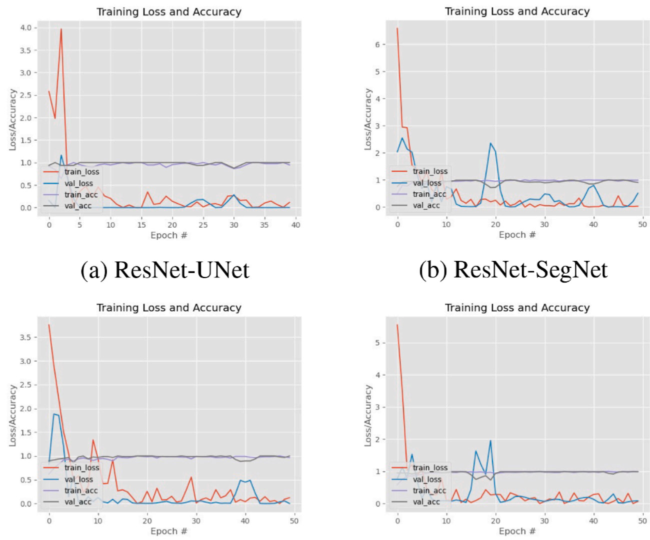

(a) ResNet-UNet (b) ResNet-SegNet

(c) VGG-SegNet (d) MobileNet-SegNet

Fig. 9. Training Accuracy and Loss Curves.

value of τ is computed through empirical evaluation.

The main framework of VBSeg comprises of image opening ($I_b^{f,a,o}$) [111] morphological operation for resolving the image region merger as shown by red-arrow in Fig. 8 (b). The major drawback observed is reduction in size of VB, however the region merger problem is addressed as shown in Fig. 8 (c). In order to preserve the edges, preservation attempt is made through application of anisotropic filtering ($I_b^{f,a,o,s}$) [19]. In the last step of main framework, shape-based filtering is performed to extract the lumbar spine VBs. Here, it is important to mention that VBs present signature shape and size with respect to other regions in lumbar spine. In order to segment the VBs, ratio of major-and minor-axis MA/mA, region extent and area are computed and a threshold (ρ) is devised through empirical evaluation. The VBs not meeting the threshold are rejected and the lumbar spine VBs are obtained (I_{VB}^{pv}) as shown in Fig. 8 (d).

In the final validation stage, the number of VBs (nVB) along the spinal curve region are checked. If the number of detected VBs are 6 ± 1, the result is accepted otherwise the region/shape-based filtering is performed again by varying the threshold (ρ) as shown in Algorithm 1. The images after post-validation stage are shown by Fig. 8 (e).

6.2. Deep Learning Method

As already covered in the literature review section, many researchers have strongly advocated the use of deep learning methods to perform segmentation tasks. We performed VBs segmentation using conventional deep learning encoder-decoder, scene parsing and mobile networks. Here, we compared multiple popular models such as UNet [98], ResNet [49], SegNet [9], PSPNet [132] and MobileNets [50]. A concise description of the models is given as follows:

- **UNet**. Originally inspired by Fully Connected Network (FCN) [67], UNet has a contraction path and an expansion path. The contraction path, of traditional convolutional neural network (CNN) and max pooling layers, preserves contextual information while the expansion path localizes information through transpose CNN. Like in ResNet, UNet also concatenates features by providing skip connections from contraction to expansion path. It has a built-in data augmentation scheme hence very well suited for limited data cases [98].
- **ResNet**. Residual Networks or ResNet solved the issue of vanishing gradient descent by introducing skip connections, thereby increasing flexibility and offering better preservation of contextual information [49].
- **SegNet** based on encode-decoder architecture, where the encoder part preserves the contextual information and decoder part uses the max-pooling indices computed in encoder part to up-sample the feature-map non-linearly. It is computationally efficient once compared to UNet, owing to its lesser number of trainable parameters [9].
- **PSPNet**. The pyramid scene parsing network makes use of pyramid pooling module to capture global contextual information, coarser to finer, in four-pyramids level. The feature-maps are up-sampled by decoder to present segmented result [132].
- **MobileNets**. MobileNets is based on depth-wise separable convolution hence, offering reduction in size of model. It is suited for implementation in embedded systems and mobile applications on the fly due to lesser size and comparable accuracy [50].

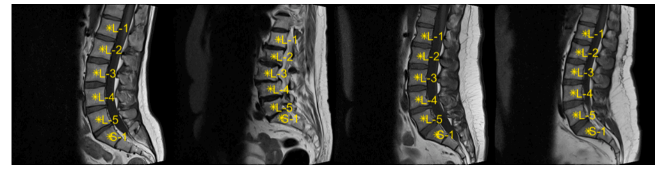

Fig. 10. VB Identification and Labelling.

The use of deep learning based architectures is widespread and are extensively found in medical image segmentation related research work [46,63,106,109,130]. We have made use of various encoder-decoder configurations by combining networks including ResNet-PSPNet [119], MobileNets-UNet [55], VGG-UNet [10], ResNet-UNet [133], ResNet-SegNet [106] and others as suggested by the researchers. All the models are trained and tested on Intel ® Xeon ® Silver 4110 CPU with 64 GB RAM and NVIDIA Quadro P4000 GPU, using Tensorflow[1] Keras API [25], Python 3.7.9 [120]. We have used Adadelta [128] optimizer with cross-entropy loss function, batch size of 2 and total 50 epochs for training; using fine-tuning. The selection is crystallized after detailed empirical evaluation. Summarized overview is presented viz:-

- In total 360 images are used to perform training session whereas 154 images (514 total images) are used for testing purpose using the ratio of 70:30.
- Fine-tuning method for transfer learning is adopted where the layers weights are fine-tuned whereas the final classification layer is trained from scratch. The obvious advantage of this method is quicker training as opposed to training the entire model from scratch and additionally offering better generalization as compared to transfer learning where only the last layer is updated.
- Adadelta optimizer is selected because it reduces the burden of selection of default learning rate η.
- Cross-entropy loss function is used as default loss function.
- The batch-size of 2 is selected experiencing better accuracy and requiring less computational resources as opposed to batch sizes of 4 and more.

We have found that training time is the least for MobileNets-SegNet i.e., an average of 42.2 s per epoch, whereas the most for VGG-UNet i.e., an average of 465 s per epoch. The best training performance for VB extraction is achieved by ResNet-UNet as depicted in Fig. 9, where the loss value is consistent as compared to other models.

7. Automated Extraction of Spinal Measurements

To evaluate the spinal misalignment disorders (Sections 2.2.1, 2.2.2), we present a fully automated scheme that quantitatively calculates the lumbar spine deformity, which serves as a handy aid for spinal surgeons to make certain decisions regarding the adoption of suitable surgical procedure. Here, we perform automated measurements two times involving the same steps as shown in the measurement acquisition scheme presented as Algorithm 2. In the first measurement process, ground truth labels which we manually created as described in Section 5 are used in order to complement the images with quantitative attributes, forming part of composite dataset. While in the second measurement sequence, the automated segmented images with best quantitative results, in our case ResNet-UNet, are used to perform spinal measurements to establish correlation with the measurements obtained on the ground truth labels.

Algorithm 2: Spinal Measurements Extraction Scheme

Input: Extracted Image (I_{VB})
Output(s): $LH_{cp}, LH_{cen}, IVB_i^a, IVB_i^p, VB_i^p, VB_i^a, LLA, LSA$
for $\forall\ VBs$ **do**
  $cen_i \leftarrow \text{ComputeCenter}(I_{VB})$
  $cp_{i,d}^{raw} \leftarrow \text{CornerPoint}(cen_i)[d = T_L, T_R, B_R, B_L]$
  $cp_{i,d} \leftarrow \text{CorrectionCP}(cp_{i,d}^{raw})[Edge, NN]$
end
$LH_{cp} \leftarrow \text{LumbarHeight}(cp_{i,T_L}) \leftarrow [L1_{T_L}, S1_{T_L}]$
$LH_{cen} \leftarrow \text{LumbarHeight}(cen_i) \leftarrow [L1, S1]$
$IVB_i^a \leftarrow \text{Distance}(cp_{i,B_L,T_L}) \leftarrow [L_{i_{B_L}}^a - L_{i+1_{T_L}}^a]$
$IVB_i^p \leftarrow \text{Distance}(cp_{i,B_R,T_R}) \leftarrow [L_{i_{B_R}}^p - L_{i+1_{T_R}}^p]$
$VB_i^a \leftarrow \text{Distance}(cp_{i,T_L,B_L}) \leftarrow [L_{i_{T_L}}^a - L_{i_{B_L}}^a]$
$VB_i^p \leftarrow \text{Distance}(cp_{i,T_R,B_R}) \leftarrow [L_{i_{T_R}}^p - L_{i_{B_R}}^p]$
$LLA \leftarrow \text{ComputeAngle}(cen_i, cp_{i,d}) \leftarrow [L1_{T_L,T_R}, S1_{T_L,T_R}]$
$LSA \leftarrow \text{ComputeAngle}(cen_i, cp_{i,d}) \leftarrow [L5_{B_L,B_R}, S1_{T_L,T_R}]$

7.1. Identification and Labelling of VB

As a first step, we perform region segmentation in order to isolate the individual VB and extract respective centroid. A subsample of result comprising of 4-images is showcased in Fig. 10. Labels are assigned from L1-L5 for lumbar VBs and S1 to the first sacrum VB and * represents the centroids.

7.2. Computation of Corner Points

After identifying the individual VB, respective corner-points are computed. Due to the variation in orientation and end-plate deformations (osteophytes), the computation of corner-points is done in a sequential manner. Initially, raw corner-points are assigned based on the corners of smallest possible bounding-box drawn around the individual VB, followed by correction sequence involving, image skeletonization and nearest-neighbor calculation. The distance is computed for each corner-point, say superior-left, superior-right, inferior-right, inferior-left, from the non-zero list of coordinates from skeletonized image. The lowest distance pixel-coordinate is assigned to the respective corner-point. The expression is given as follows:

$$d_{\tau,i} = \sqrt{p_\tau^2 - p_i'^2} \tag{1}$$

where, p_τ represents the raw corner-points assigned by the corners of bounding box and the sub-script τ depicts the four-corner points namely superior-left, superior-right, inferior-right, inferior-left, p_i' shows all the non-zero pixels of a particular VB, $d_{\tau,i}$ shows the distance matrix for all four corner points. Finally, the minimum distance pixel index as given in Eq. 2 is stored and the coordinate corresponding to the index (idx) is assigned to the respective corner-point p_τ.

$$idx = \min(d_{\tau,i}), p_\tau \leftarrow p_{idx}' \tag{2}$$

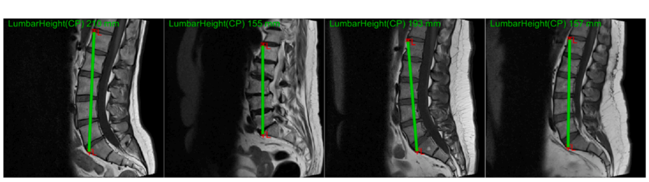
(a) Measured between L1-S1 Anterior-Superior Corner-Points.

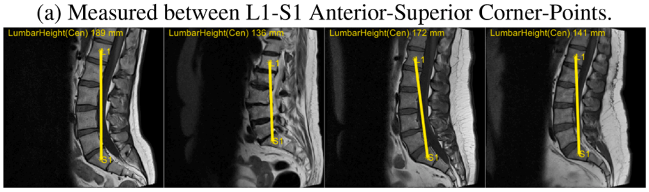
(b) Measured between L1-S1 Centroids.

Fig. 11. Calculation of Lumbar Height in *mm*.

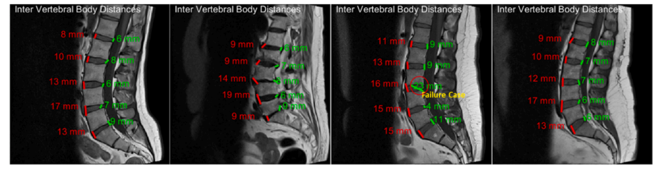

(a) IVB Distances.

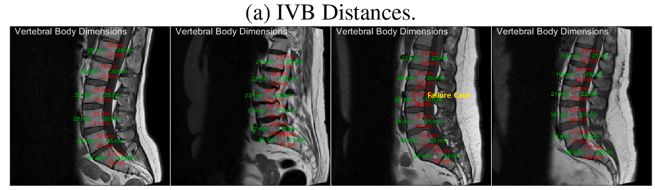

(b) VB(s) Side-Wall Dimensions.

Fig. 12. Calculation of Intervertebral body (IVB) distances and VB Dimensions in *mm*.

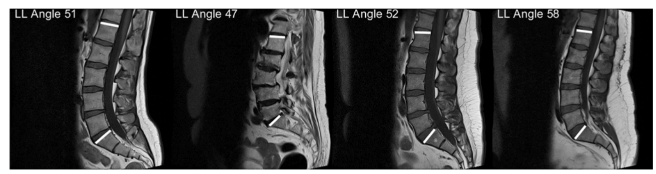

(a) Lumbar Lordotic Angle (LLA).

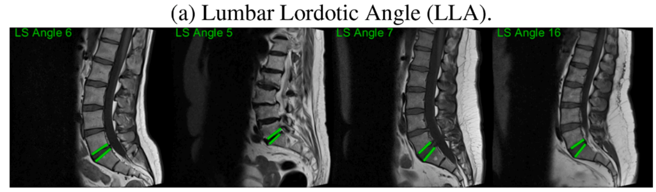

(b) Lumbosacral Angle (LSA).

Fig. 13. Spinal Angular Measurements measured in Degrees (∘).

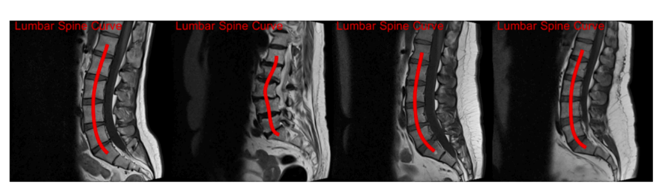

Fig. 14. Estimation of Spinal Curve.

7.3. Distance Related Measurements

After calculation of 4 corner points, *lumbar height* is computed based on the Euclidean distance using two different approaches. In the first method, distance between L1 superior-anterior corner point and S1 superior-anterior corner-point as shown with green line segment in Fig. 11 (a). In the second method, the lumbar height is measured from centroids between L1 VB and S1 VB as depicted by the yellow line segment in Fig. 11 (b).

Intervertebral body distances (IVB) i.e., distance between consecutive VB at anterior and posterior sides is also measured. While computing the distances at anterior side of the spine, the distance between anterior-inferior corner point and anterior–superior corner point of consecutive VB is measured. Similar measurement is performed for posterior sides as shown in Fig. 12 (a). Here, the measurements represented in red are anterior side measurements, whereas the posterior side measurements are given in green font.

Likewise, the *VB dimension* are measured at anterior and posterior sides such that the distances between the superior and inferior corner points are measured in the same VB as depicted in Fig. 11 (b). A failure case (2^{nd} sub-image from right) is also showcased in Fig. 11 labelled in yellow, where the computation error is due to the misalignment of corner point. All the distance related measurements are calculated using the expression given in Eq. 3 for Euclidean distance given below

$$d = \sqrt{(x_2 - x_1)^2 + (y_2 - y_1)^2} \tag{3}$$

In both cases, the lumbar height(s), IVB distances and VB dimensions are measured in millimeters *mm*.

7.4. Angular Measurements

After computing the distance related measurements, angular measurements are also performed. First, *lumbar lordotic angle (LLA)*, being the angle subtended by L1 superior-endplate and S1 superior-endplate, is measured as represented by white lines in Fig. 13 (a). The expression is given as

$$m^{L1,S1} = \frac{y_2^{L1,S1} - y_1^{L1,S1}}{x_2^{L1,S1} - x_1^{L1,S1}} \tag{4}$$

where in Eq. 4, $m^{L1,S1}$ depict slopes of two line segments i.e., L1 superior-endplate and S1 superior-endplate. The angle θ is calculated using the expression given in Eq. 5 below

$$\theta = \tan^{-1}\left|\frac{m^{L1} - m^{S1}}{1 + m^{L1}m^{S1}}\right| \tag{5}$$

In the similar manner, *LSA*, angle subtended by the L5 inferior end-plate and S1 superior end-plate is also measured as shown in Fig. 13 (b) where the green lines depict the L5 inferior-endplate and S1 superior-endplate. The measured angles are also labelled in both cases for LLA and LSA.

7.5. Spinal Curve Estimation

Lumbar spinal curve is also plotted to differentiate between the symmetrical and asymmetrical spinal curves and to support the subsequent spinal disorder diseases classification methodologies. Here, cubic spline interpolation is used instead of polynomial piecewise interpolation to avoid the higher order polynomials hence avoiding overfitting and enabling better generalization of spinal curve. In the case of lumbar spine, spline fitting is performed on previously identified centroids. The result of curve estimation is shown in Fig. 14 (2^{nd} sub-image from left), it can be seen that the slope in asymmetrical giving evidence that spinal balance is out of order, whereas in the other shown sub-images the curves are found to be symmetrical.

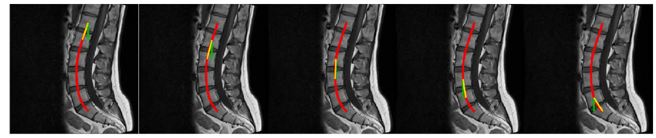

Fig. 15. Angular Deviation Metric for Assessment of Spondylolisthesis.

Since, all these distance related measurements are in pixels which are made meaningful and relatable by conversion of these distances into millimeters. For this purpose, the respective pixel spacing information is extracted from the DICOM file and the distance in pixels are scaled as per the pixel spacing information.

8. Spinal Misalignment Disease(s) Classification

After extracting the spinal profiles, including spinal measurements (7.3, 7.4) and spinal curve estimation(7.5), we propose novel methodologies for spinal misalignment(s) classification.

8.1. Automated Spondylolisthesis Classification

As already covered in the Section 2.2.1, for grading of severity and determining etiological type of spondylolisthesis, Meyerding classification grading system is commonly used. The clinicians mostly resort to grading by visual observation, without performing the measurements. Quite evidently, this methodology for grading is subjective in nature, therefore, automated quantitative assessment is necessitated. In this paper, we introduce a novel technique to identify and classify spinal misalignment i.e., spondylolisthesis by using an improved angular deviation metric. The algorithmic representation is given as Algorithm 3, where the segmented VB image serves as input image (I_{VB}) and a class label i.e., (ω_i) for respective VB is the output. The value of ω_i ranges from normal to presence of spondylolisthesis in either anterior or posterior direction.

Algorithm 3: Spondylolisthesis Classification

Input: Extracted Image (I_{VB})
Output: *Classification* (ω_i)
$cen_i \leftarrow$ ComputeCentroids(I_{VB}) [$i = n_{VB}$]
$\theta_{i-1} \leftarrow$ ComputeAngle(cen_i)
$\theta_m \leftarrow$ ComputeMean(θ_{i-1})
$\sigma_\theta \leftarrow$ ComputeSD(θ_{i-1})
for $\forall\ cen_i$ **do**
  if $\angle_i > \theta_m + \sigma_\theta$ **then**
    $\omega_i^{anterior} \leftarrow I_{VB_i}$
  else
    if $\angle_i < \theta_m - \sigma_\theta$ **then**
      $\omega_i^{posterior} \leftarrow I_{VB_i}$
    else
      if $\theta_m - \sigma_\theta < \angle_i < \theta_m + \sigma_\theta$ **then**
        $\omega_i^{normal} \leftarrow I_{VB_i}$
      end
    end
  end
end
$\omega_i \leftarrow \omega_i^{anterior}$
$\omega_i \leftarrow \omega_i^{posterior}$
$\omega_i \leftarrow \omega_i^{normal}$

In our proposed method, instead of the original method used by

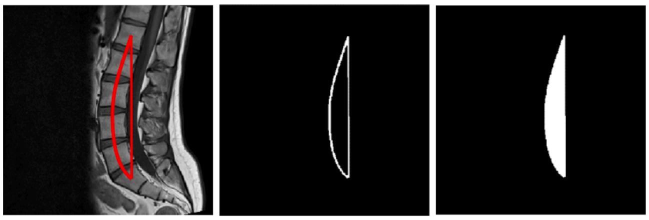

(a) Region Plot (b) Segmentation (c) Area Computation

Fig. 16. Proposed AUC Method for LL Assessment.

Algorithm 4: Hyper/Hypo/Normal Lordosis Classification

Input: Extracted Image I_{VB}
Output: *Classification* ω
$cen_i \leftarrow \mathrm{ComputeCentroids}(I_{VB})\ [i = nVB]$
$Curve \leftarrow \mathrm{SpinalCurve}(cen_i)$
$R \leftarrow \mathrm{MakeRegion}(Curve)$
$A_R \leftarrow \mathrm{Area}(R)$
$\phi \leftarrow \mathrm{Range}(A_r)[a, b]$
if $A_r > \phi$ **then**
    $\omega_{hyper} \leftarrow I_{VB}$
else
    if $A_r < \phi$ **then**
        $\omega_{hypo} \leftarrow I_{VB}$
    else
        if $A_r = \phi$ **then**
            $\omega_{normal} \leftarrow I_{VB}$
        end
    end
end
$\omega \leftarrow \omega_{hyper}$
$\omega \leftarrow \omega_{hypo}$
$\omega \leftarrow \omega_{normal}$

clinicians to measure spondylolisthesis which is based on corner-points and related to end-plate structure; evaluation for presence of spondylolisthesis through centroids (cen_i) is performed, thus harnessing the potential of automated measurements and the previously computed centroids (7.1) and corner-points(7.2).

As shown in Fig. 15, initially beginning from L1 VB (left), the angle (θ_{i-1}) subtended between perpendicular line (shown in green) from L1 centroid and the line segment from L1 centroid to L2 centroid (shown in yellow) is measured. The process is repeated for all the VBs from L2 to S1 as shown in Fig. 15left to right). Intuitively, it can be seen that if the angle of respective VB is found deviating beyond the standard deviation (σ_θ) of the mean of angles (θ_m) of all VBs, the VB is classified to have dislocation i.e., spondylolisthesis or mathematically as shown in Eq. 6 given below:

$$\omega_i = \frac{1}{n}\sum_{i=1}^{n}\theta_i \pm \sigma_\theta \tag{6}$$

where, θ_i is the angular deviation measured between the yellow and green lines as shown in Fig. 15 (left to right), $n = 5$ i.e., the number of VBs segments and σ_θ is the measure of standard deviation. The dislocated VB is then assigned with the label ω_i.

A noticeable *advantage* in proposed angular deviation classification metric, is the ability to handle displacement of VB in both posterior and anterior directions. The present-day method used by clinicians to evaluate spondylolisthesis is based on posterior-inferior corner-points [32] as already referred and shown in Fig. 1. In this proposed algorithm, the posterior or backwards displacement ($\omega_i^{posterior}$) is quantified, if the angular deviation is less than the standard deviation of mean of all deviation angles, similarly, the anterior or forward displacement ($\omega_i^{anterior}$) is conditional to the deviation beyond the standard deviation of mean of all angles as highlighted in the Algorithm 3.

8.2. *Automated Lumbar Lordosis Assessment*

For assessment of LL, modified Cobb method is used by the clinicians which is related to the superior and inferior VB end-plates, hence, in case of deformation or fracture correct lordosis assessment may not be possible. Exploiting the potential of reliable methods [124] for lumbar spine lordosis evaluation, not involving the end-plate structures, our proposed method is a combination of Chen [23] centroid method and Yang et al. [126] AUC method.

In our proposed method (Algorithm 4), spinal curve is plotted (Fig. 16 (a)) through the centroids (cen_i) instead of posterior corner-points in the original Yang et al. [126] method. Afterwards, the superior VB centroid is connected directly to inferior VB centroid and area enclosed in the region (A_R) is computed (Fig. 16 (a), (b)) in the similar pattern as suggested in Yang method. Clinically, it is established that normal lordosis ranges from 39° - 53° [92], where the curvature is termed as hyper-lordosis if the angle exceeds 53° and hypo-lordosis if the angle is less than 39°. The same is empirically evaluated and a correlation is established for area of region (A_R), hence defining a range (ϕ) for normal-lordosis.

The expression is given as Eq. 7, which is the summation of all non-zero pixels ($p_i \neq 0$) within the region r as shown in Fig. 16 (c), where the total number of non-zero pixels are m and Δp is the interval i.e., equal to one pixel.

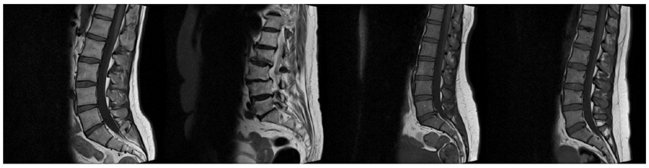

(a) Input Images.

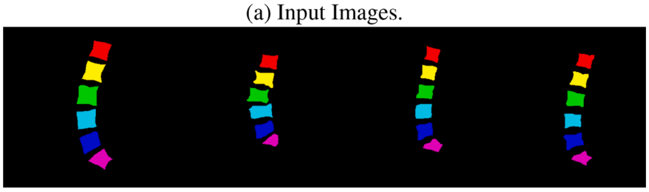

(b) Ground Truth Images.

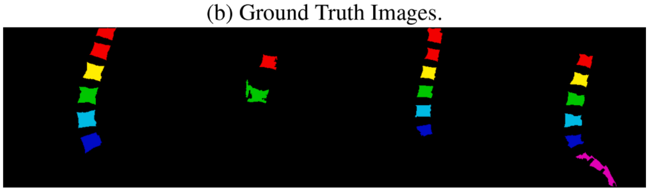

(c) Result of VBSeg (Proposed Conventional Algorithm).

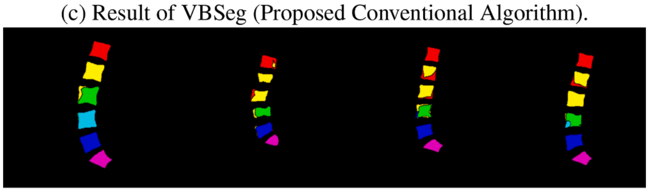

(d) Adopted Architecture ResNet-UNet.

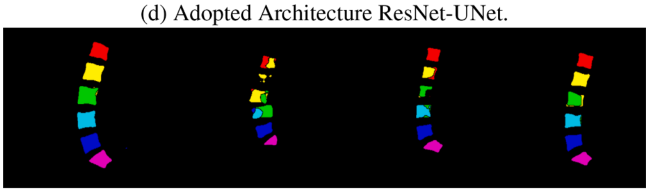

(e) VGG-SegNet Architecture.

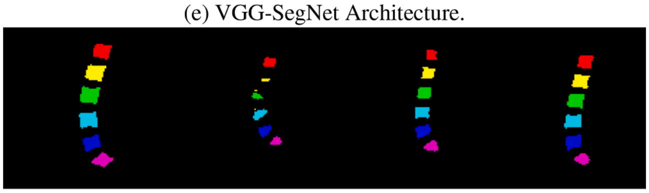

(f) MobileNets-SegNet Architecture.

Fig. 17. Qualitative Comparison of VB Segmentation Results.

Table 1
Comparative Quantitative Analysis of Methods/Models used for Semantic Segmentation.

	MPA	MPP	IoU	DSC
VBSeg (Pre-Validation)	96.34	57.46	0.49	0.67
VBSeg (Post-Validation)†	97.99	66.57	0.63	0.79
UNet	98.36	90.67	0.74	0.87
PSPNet	98.33	88.95	0.73	0.80
VGG-UNet	99.02	87.29	0.82	0.93
VGG-PSPNet	97.85	91.85	0.69	0.69
VGG-SegNet*	98.85	95.41	0.81	0.95
ResNet-UNet*	**99.12**	**98.31**	**0.86**	**0.97**
ResNet-PSPNet	98.08	95.66	0.72	0.76
ResNet-SegNet	98.59	98.06	0.78	0.93
MobileNets-UNet↓	97.50	81.33	0.67	0.63
MobileNets-SegNet*	98.63	88.71	0.75	0.87

$$A_r = \sum_{i=1}^{m} p_i \times \Delta p \quad (7)$$

For assessment of lordosis, the proposed method, based on AUC computation is independent of corner-points hence, is more robust to the end-plate deformities.

9. Results and discussion

In this section, first we present the metrics which are used to validate the performance of the automated VB extraction i.e., segmentation, automated spinal measurements and spinal diseases classification. The same are extensively used by the research community [13,30,41,52,48,81,117,82,131] Afterwards, category wise detailed experimental results with qualitative and quantitative analysis are highlighted in subSections 9.1, 9.2 and 9.3.

To evaluate the performance of **semantic segmentation**, *mean pixel accuracy (MPA)* and *mean pixel precision (MPP)* metrics as given in Eqs. 8 and 9 are used. Accuracy corresponds to the measure of percentage of pixels classified correctly in global context as VB and background, whereas, precision is the measure of correctness of classification at global level.

$$MPA = \frac{T_P + T_N}{T_P + T_N + F_P + F_N} \quad (8)$$

$$MPP = \frac{T_P}{T_P + F_P} \quad (9)$$

where, T_P denotes the pixel-level true positives indicating the correct extraction of VBs, T_N relates to pixel-level true negatives showing correct assignment of pixels as background, F_P signifies the pixel-level false positives indicating incorrect extraction of background pixels as VB and F_N specifies the false negatives i.e., incorrect extraction of VB pixel labels.

To measure the **overlap** between the segmented mask and the actual ground truth mask, mean *intersection-over-union (IoU)* commonly termed as Jaccard similarity coefficient score is used, which is measured through Eq. 10.

$$IoU = \frac{T_P}{T_P + F_P + F_N} \quad (10)$$

Additionally, *dice similarity coefficient (DSC)* score is also computed which computes the IoU/Jaccard metric with the only difference that it doubles the true-positives T_P, expression is given as Eq. 11.

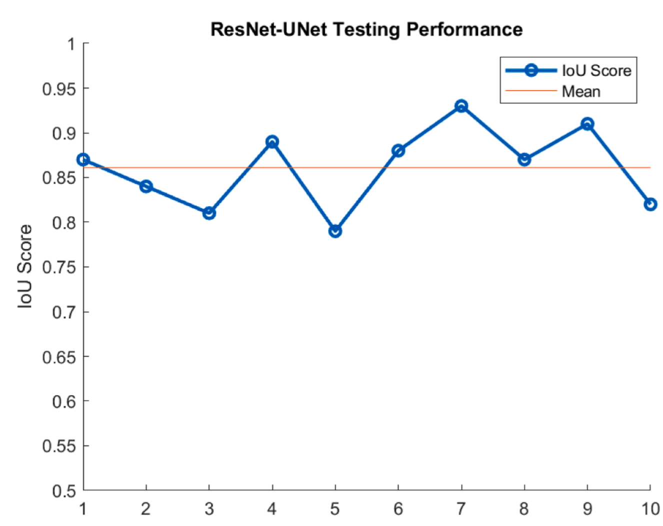

Fig. 18. ResNet-UNet Testing Performance.

Table 2
Comparison of Segmentation Results with related Researchers' Work.

	Method	IM	MPA	MPP	IoU	DSC
Adopted Method	ResNet-UNet	MR	**99.12**	**98.31**	0.86	**0.97**
Suzani et al. [116]	6-FFN	CT	96	94.4	–	–
Lu et al. [68]	UNet	MR	94	–	0.91	0.93
Janssens and Zheng [54]	FCN-UNet	CT	–	–	–	0.95
Lessmann et al. [61]	FCN	MR/CT	–	–	–	0.94/0.96
Rak et al. [96]	UNet	MR	–	–	–	0.94
Huang et al. [52]	UNet	MR	–	–	**0.94**	–
Tang et al. [118]	DDUNet	CT	90.1	–	0.83	–

$$DSC = \frac{2T_P}{2T_P + F_P + F_N} \tag{11}$$

Furthermore, to measure of **closeness** of the automated measured value with the manual measurement performed by spinal surgeons, *Pearson correlation coefficient* is used as given in Eq. 12,

$$R = \frac{\sum_{i=1}^{N}(m_i - \overline{m})(n_i - \overline{n})}{\sqrt{\sum_{i=1}^{N}(m_i - \overline{m})^2 \sum_{i=1}^{N}(n_i - \overline{n})^2}} \tag{12}$$

where, R is the correlation coefficient, N is the total number of observations, m_i is the automated calculated measurement taken for a specific sample i, $\overline{m}$ is the mean value of automated computed measurement, n_i is manual computer assisted measurement performed by the spinal surgeon for a specific sample i, $\overline{n}$ is the mean of manual measurement performed by the spinal surgeon. Its value ranges from -1 to 1 where the value $(R = 0)$ means that the measurements are not correlated.

Similarly, to measure the **errors** in the predicted or estimated value without considering the direction of error mean *absolute error metric (MAE)* is computed. The expression given in Eq. 13:

$$MAE = \frac{1}{N}\sum_{i=1}^{N}|x_i - \overline{x_i}| \tag{13}$$

which shows that x_i is the computer assisted measurement performed by the spinal surgeon and $\overline{x_i}$ is the automated measurement. The average value gives the estimate of error value giving individual difference equal weight.

9.1. Segmentation of VBs

The qualitative results are shown in Fig. 17, followed by detailed quantitative assessment as given in Table 1. In the figure, the sub-captions are also mentioned below each row showcasing the type of images. Here, we present a selected pictorial comparison of results obtained by our proposed VBSeg algorithm with the segmentation results obtained through various deep learning networks. A row represents results of a single scheme on various samples whereas a column represents the results with different model/methods for a specific sample. A failure case is also presented in second column from left where it can be seen that VBSeg totally misses the VBs, whereas the deep learning methods have shown promising results. It can also be seen that ResNet-UNet conveniently outperforms the results obtained by other deep learning networks including original proposed VBSeg, despite the fact VBSeg is a customized thoroughly worked-out algorithm to perform VB segmentation task.

Similarly, while analyzing the quantitative aspects in Table 1, it is quite evident that, the validation sequence used in VBSeg (*VBSeg*$^{\uparrow}$) shows improvement in metrics, but is unable to reach anywhere near the results of best segmentation metrics obtained through deep learning networks. Amongst the deep learning networks, quite obviously, the lowest quantitative metrics are given by MobileNets-*UNet*$^{\downarrow}$ with the lowest training time. The results of *VBSeg*$^{\uparrow}$ are comparable to MobileNets-UNet$^{\downarrow}$ with respect to achieved IoU and DSC scores. In Table 1, mean pixel accuracy is represented by MPA, mean pixel precision by MPP, intersection over union is given by IoU whereas dice similarity coefficient score is given by DSC. Additionally, * marks with the models represents the best results within the same base-model category i.e., VGG, ResNet, MobileNets. The overall best results are given in bold

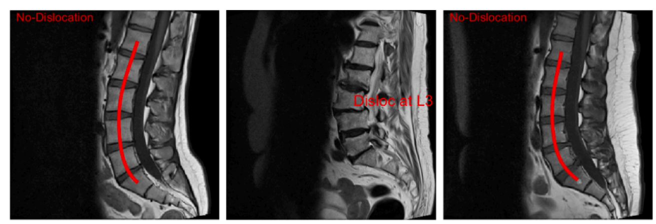

(a) No Dislocation (b) Dislocation at L3 (c) No Dislocation

Fig. 19. Results of Spondylolisthesis Classification.

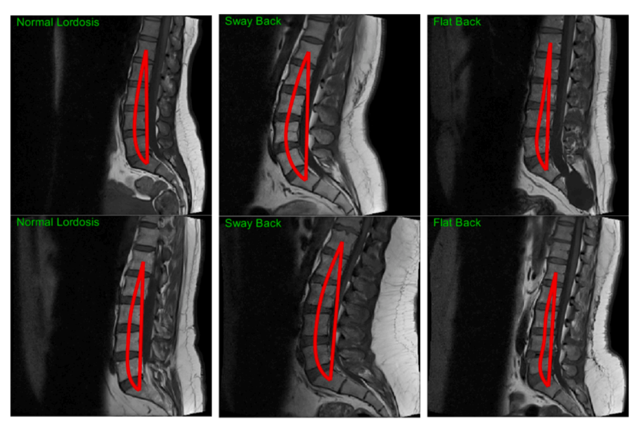

(a) No Dislocation (b) Dislocation at L3 (c) No Dislocation

Fig. 20. Automated LL Assessment Result.

Table 3
Spinal Measurements Quantitative Comparison.

	LLA		LSA		LHCP		LHC	
	R %	MAE θ°	R %	MAE θ°	R %	MAE mm	R %	MAE mm
GT-SS	**0.979**	**1.45**	**0.951**	**1.55**	**0.997**	**0.82**	**0.996**	**0.89**
GT-DL	0.84	2.61	0.79	2.01	0.981	1.07	0.992	0.95
SS-DL	0.81	3.63	0.83	3.16	0.978	1.2	0.991	0.92
Masad et al. [73]	0.932	–	–	–	–	–	–	–
Pang et al. [89]	–	–	–	–	–	1.23	–	–
Cho et al. [24]	–	8.05	–	–	–	–	–	–

whereas the worst result in the deep learning category are given by ↓ as marked with MobileNets-UNet. Here, it is also important to mention that MPA and MPP values are ranging from 0 to 100 where a value close to 100 is signifying better performance. Similarly, the values of IoU and DSC are ranging between 0 to 1, where, a value close to 1 represents a better performance of the model/method. The IoU score of ResNet-UNet model for 10 iterations depicting the testing performance as showcased in Fig. 18. Here the red line is highlighting the mean value of 0.86 with a standard deviation of 0.04.

In Table 2, we present a comparison of results obtained with our adopted method i.e., ResNet-UNet architecture with the results of various researchers using deep learning models on different datasets. The image modality (IM) and the method or technique adopted by respective researcher is also mentioned. The significance of this table is to enable the reader in establishing confidence in adoption of ResNet-UNet architecture to perform semantic segmentation task for extraction of lumbar VBs. Clearly, the results obtained by the adopted method are comparable with the results achieved by other researchers in accuracy, precision, IoU and DSC. In literature, the reported range for MPA and MPP is also from 0 to 1, however, the value is scaled between 1 to 100 in order to avoid confusion. The values of IoU and DSC are within the range from 0 to 1, where the value near to zero shows that very less overlap is present between the ground truth and segmented image and the value near to one represents a good overlap.

9.2. Spinal measurements

The qualitative aspects of spinal measurements are amply covered and elaborated in Section 7 as shown in Figs. 10–13. To quantitatively analyze the results of measurements, out of the total 514 images, a sample of 50 images are randomly picked and are manually measured by spinal surgeon using RadiAnt DICOM Viewer by Medixant [76].

The results are reported in Table 3, where, R is the correlation coefficient while MAE is mean absolute error, lumbar lordotic angle is referred as LLA, lumbosacral angle as LSA, lumbar heights (corner points) is given as LHCP refer to superior-anterior corner-point of L1 to superior-anterior point S1, lumbar heights (center points) is given as LHC refer to center point of L1 and S1. Moreover, bold indicates the best performance while '-' indicates that the metric was not been computed by the researcher.

GT-SS represents comparison between measurements of ground truth images and measurements of spinal surgeon, GT-DL shows the comparison between measurements of ground truth images and measurements of automated segmented out image using deep learning method (ResNet-UNet) and finally, SS-DL means establishing relationship between the measurements of spinal surgeon and automated segmented out image using deep learning model (ResNet-UNet).

It can be seen that the proposed scheme achieves a correlation coefficient of *0.979* with the clinician's grading (with the MAE of 1.45°) for the LLA. Comparing it with the state-of-the-art schemes, the proposed framework achieved an improvement of *4.80* % (in terms of R). Although this comparison is indirect as the clinician's and their gradings in all the schemes varies. Nevertheless, it is worth noting that the spinal measurement obtained through the proposed scheme highly correlates (being statistically significant i.e. ($p < 0.05$) with the expert clinicians as evident through R and MAE scores. Moreover, unlike its competitors, the proposed framework is also capable to measure LSA, and lumbar heights as evident from Table 3.

9.3. Spinal disorders classification

In this subsection, the results of two-proposed spinal disorder diseases classification methods including spondylolisthesis and classification for hyper/hypo/normal lordosis cases are presented.

9.3.1. Spondylolisthesis

Based on the manual radiologist report, out of total 514 patients, 29 candidate patients were diagnosed with presence of spondylolisthesis with variation of grade. The proposed automated disease classification system achieved the accuracy of *89 %* following the improvised angular deviation criteria, which was covered in details in Section 8.1. A few selected results are displayed as sub-images in Fig. 19, where it can be seen that the classification model correctly identifies and labels the spinal dislocation disorder showcased by 'Disloc at L3' as shown in Fig. 19 (b). The proposed Algorithm 3 also correctly categorized the normal cases labelled as 'No-Dislocation' as shown in Fig. 19 (a), (c).

9.3.2. Lumbar lordosis assessment

As already emphasized in Section 8.2, the proposed method harnessed the accuracy of computed centroids as advocated by Chen [23] method, as evaluation with the help of corner-points is subjective to errors in measurement, and made use of technique of computing area in an enclosed region (A_r) in a similar way as suggested in Yang et al. [126] method.

Through meticulous experimentation, it is found that area of region (A_r) for hypo lordosis/ straight-back/ flat-back cases is smaller once compared to normal lordosis. Similarly, the area of region (A_r) for hyper lordosis/ sway-back is greater than a normal lordosis curve, the same result were presented in the original AUC method[126]. The proposed automated spinal disorder classification system achieved an accuracy of *93 %* correctly identifying straight-back, sway-back (disorder cases, combined) and identifying the normal lordosis cases. Result of proposed Algorithm 4 for automated lordosis assessment is presented in Fig. 20. Here, a sub-sample of results (6-images) is displayed where the normal lordosis are shown in sub-Fig. 20 (a), sway-back or hyper lordosis cases in sub-Fig. 20 (b) and flat-back or hypo lordosis cases in sub-Fig. 20 (c).

The clinicians, at present, use Meyerding classification to grade the severity of spondylolisthesis, which is certainly subjective. Our proposed method uses an improvised angular deviation metric to identify the presence of this disorder. Likewise, the clinicians identify adequacy/ inadequacy of LL through modified Cobb angle, which is dependent on the structure of superior and inferior VB end-plates. The method proposed in this thesis is based on area calculation by creating a region through centroids instead of corner-points.

10. Conclusion

To conclude, in this paper, we have presented a composite dataset comprising of highly detailed annotations of mid-sagittal views of lumbar spine MR images coupled with spinal measurements, rendering quantitative assessment of lumbar spine misalignments. Furthermore, we presented an autonomous framework capable of extracting the spinal measurements on-the-fly which can aid the clinicians in objectively assessing the spinal pathology of the candidate subject. Additionally, this paper also introduced fully automated classification of spinal disorders such as spondylolisthesis, sway-back/flat-back cases. Certainly, the intended purpose of proposed autonomous lumbar spine toolkit is not to replace the role of clinicians but to introduce a vote of confidence and reliability to their performed manual diagnosis. With the adoption of our toolkit, clinicians may enable themselves with reliable quantitative metrics thereby adding precision to the selected/shortlisted surgical intervention procedure. In future, the proposed framework can be extended to objectively measure the misalignment within the cervical, thoracic, and pelvic region as well to give more in-depth understanding of the human spinal balance. Another direction which may be explored is determining of the efficacy of automated spinal toolkit in aiding the spinal surgeons to choose less invasive method over extensive invasive methods.

Declaration of Competing Interest

The authors declare that they have no known competing financial interests or personal relationships that could have appeared to influence the work reported in this paper.

Acknowledgements

We would like to thank Sudirman et al. [114] for giving us formal permission to share and redistribute the original dataset, after our mid-sagittal views annotations. We would also like to thank our families for rendering us the due support and encouragement in carrying out this research. We also acknowledge the efforts of volunteer expert clinicians including both radiologists and spinal surgeons.

Funding Information: This research was not funded by any organization.

References

[1] M. Abadi, A. Agarwal, P. Barham, E. Brevdo, Z. Chen, C. Citro, G.S. Corrado, A. Davis, J. Dean, M. Devin, S. Ghemawat, I. Goodfellow, A. Harp, G. Irving, M. Isard, Y. Jia, R. Jozefowicz, L. Kaiser, M. Kudlur, J. Levenberg, D. Mané, R. Monga, S. Moore, D. Murray, C. Olah, M. Schuster, J. Shlens, B. Steiner, I. Sutskever, K. Talwar, P. Tucker, V. Vanhoucke, V. Vasudevan, F. Viégas, O. Vinyals, P. Warden, M. Wattenberg, M. Wicke, Y. Yu, X. Zheng, TensorFlow: Large-scale machine learning on heterogeneous systems, 2015. https://www.tensorflow.org/. software available from tensorflow.org.

[2] L. Agisoft, R. St Petersburg, Agisoft Metashape 1.6.5. https://www.agisoft.com/downloads/installer/.

[3] A.S. Al-Kafri, S. Sudirman, A. Hussain, D. Al-Jumeily, F. Natalia, H. Meidia, N. Afriliana, W. Al-Rashdan, M. Bashtawi, M. Al-Jumaily, Boundary Delineation of MRI Images for Lumbar Spinal Stenosis Detection Through Semantic Segmentation Using Deep Neural Networks, IEEE Access 7 (2019) 43487–43501, https://doi.org/10.1109/ACCESS.2019.2908002.

[4] M.A. Alvi, A. Sebai, Y. Yolcu, W. Wahood, B.D. Elder, T. Kaufmann, M. Bydon, Assessing the Differences in Measurement of Degree of Spondylolisthesis Between Supine MRI and Erect X-Ray: An Institutional Analysis of 255 Cases, Oper. Neurosurg. (2019), https://doi.org/10.1093/ons/opz180.

[5] S. Ansari, M. Amanullah, K. Ahmad, R.K. Rauniyar, Pott's spine: Diagnostic imaging modalities and technology advancements, 2013. doi:10.4103/1947-2714.115775.

[6] M.S. Aslan, A. Shalaby, A.A. Farag, Vertebral body segmentation using a probabilistic and universal shape model, IET Comput. Vis. 9 (2015) 234–250, https://doi.org/10.1049/iet-cvi.2013.0154.

[7] E.K. Ba, D. Gendelberg, In Brief Classification in Brief: The Meyerding Classification System of Spondylolisthesis, Clin. Orthop. Relat. Res. 478 (2020) 1125–1130, https://doi.org/10.1097/CORR.0000000000001153.

[8] E. Babai, A. Khodamoradi, Z. Mosavi, S. Bahari, An innovative software method for measuring lumbar lordosis, Ann. Biol. Res. 3 (2012) 204–213.

[9] V. Badrinarayanan, A. Kendall, R. Cipolla, SegNet: A Deep Convolutional Encoder-Decoder Architecture for Image Segmentation, IEEE Trans. Pattern Anal. Mach. Intell. 39 (2017) 2481–2495, https://doi.org/10.1109/TPAMI.2016.2644615.

[10] C. Balakrishna, S. Dadashzadeh, S. Soltaninejad, Automatic detection of lumen and media in the IVUS images using u-net with VGG16 encoder. CoRR abs/1806.07554, 2018. http://arxiv.org/abs/1806.07554, arXiv:1806.07554.

[11] C.G. Bampis, A.C. Bovik, M.K. Markey, K.M. Webb, Segmentation and extraction of the spinal canal in sagittal MR images, in: 2016 IEEE Southwest Symposium on Image Analysis and Interpretation (SSIAI), IEEE, 2016, https://doi.org/10.1109/SSIAI.2016.7459161.

[12] E. Been, L. Kalichman, Lumbar lordosis, Spine J. 14 (2014) 87–97, https://doi.org/10.1016/j.spinee.2013.07.464.

[13] B. Benjdira, K. Ouni, M.M. Al Rahhal, A. Albakr, A. Al-Habib, E. Mahrous, Spinal cord segmentation in ultrasound medical imagery, Appl. Sci. (Switzerland) 10 (2020), https://doi.org/10.3390/app10041370.

[14] H. Bennani, B. McCane, J. Cornwall, Three Dimensional (3D) Lumbar Vertebrae Data Set, Data Sci. J. 15 (2016), https://doi.org/10.5334/dsj-2016-009.

[15] S. Berven, R. Wadhwa, Sagittal alignment of the lumbar spine, Neurosurg. Clin. N. Am. 29 (2018) 331–339, https://doi.org/10.1016/j.nec.2018.03.009.

[16] D. Borenstein, A. Calin, Fast Facts: Low Back, Pain (2012), https://doi.org/10.1159/isbn.978-1-908541-16-1.

[17] D. Bradley, G. Roth, Adaptive Thresholding using the Integral Image, J. Graphics Tools 12 (2007) 13–21, https://doi.org/10.1080/2151237X.2007.10129236.

[18] E. Burian, A. Rohrmeier, S. Schlaeger, M. Dieckmeyer, M.N. Diefenbach, J. Syväri, E. Klupp, D. Weidlich, C. Zimmer, E.J. Rummeny, D.C. Karampinos, J.S. Kirschke, T. Baum, Lumbar muscle and vertebral bodies segmentation of chemical shift encoding-based water-fat MRI: the reference database MyoSegmenTUM spine, BMC Musculoskeletal Disorders 20 (2019) 152, https://doi.org/10.1186/s12891-019-2528-x.

[19] C. Bustacara, M. Gómez-Mora, L. Flórez-Valencia, Anisotropic Diffusion for Smoothing: A Comparative Study, 2016. 10.1007/978-3-319-46418-3_10.

[20] J. Carballido-Gamio, S.J. Belongie, S. Majumdar, Normalized cuts for spinal MRI segmentation, in: CARS 2002 Computer Assisted Radiology and Surgery, Springer Berlin Heidelberg, Berlin, Heidelberg, 2002, p. 1054, https://doi.org/10.1007/978-3-642-56168-9_212.

[21] J.A. Carrino, J.D. Lurie, A.N.A. Tosteson, T.D. Tosteson, E.J. Carragee, J. Kaiser, M.R. Grove, E. Blood, L.H. Pearson, J.N. Weinstein, R. Herzog, Lumbar Spine: Reliability of MR Imaging Findings, Radiology 250 (2009), https://doi.org/10.1148/radiol.2493071999.

[22] V.E. Casiano, A.M. Dydyk, M. Varacallo, Back pain. StatPearls [Internet], 2020. https://www.ncbi.nlm.nih.gov/books/NBK538173/.

[23] Y.L. Chen, Vertebral centroid measurement of lumbar lordosis compared with the Cobb technique, Spine 24 (1999) 1786–1790, https://doi.org/10.1097/00007632-199909010-00007.

[24] B.H. Cho, D. Kaji, Z.B. Cheung, I.B. Ye, R. Tang, A. Ahn, O. Carrillo, J.T. Schwartz, A.A. Valliani, E.K. Oermann, V. Arvind, D. Ranti, L. Sun, J.S. Kim, S.K. Cho, Automated Measurement of Lumbar Lordosis on Radiographs Using Machine Learning and Computer Vision, Global Spine J. 10 (2020) 611–618, https://doi.org/10.1177/2192568219868190.

[25] F. Chollet, et al., Keras, 2015. https://keras.io.

[26] S.W. Chun, C.Y. Lim, K. Kim, J. Hwang, S.G. Chung, The relationships between low back pain and lumbar lordosis: a systematic review and meta-analysis, Spine J. 17 (2017), https://doi.org/10.1016/j.spinee.2017.04.034.

[27] C. Clarke, DICOM viewers, 2018.

[28] C. Colosimo, M. Pileggi, A. Pedicelli, G. Perotti, A.M. Costantini, Diagnostic Imaging of Degenerative Spine Diseases: The Technical Approach, in: Minimally Invasive Surgery of the Lumbar Spine. Springer, London, London, 2014, pp. 21–47. DOI: 10.1007/978-1-4471-5280-4_2.

[29] C. Colosimo, M. Pileggi, A. Pedicelli, G. Perotti, A.M. Costantini, Diagnostic Imaging of Degenerative Spine Diseases: The Technical Approach, in: Minimally Invasive Surgery of the Lumbar Spine. Springer, London, London, 2014. DOI: 10.1007/978-1-4471-5280-4_2.

[30] G. Csurka, D. Larlus, F. Perronnin, What is a good evaluation measure for semantic segmentation? BMVC 2013 – Electronic Proceedings of the British Machine Vision Conference 2013, 2013. 10.5244/C.27.32.

[31] D. Czaprowski, Ł. Stoliński, M. Tyrakowski, M. Kozinoga, T. Kotwicki, Non-structural misalignments of body posture in the sagittal plane, Scoliosis Spinal Disorders 13 (2018) 6, https://doi.org/10.1186/s13013-018-0151-5. URL: https://pubmed.ncbi.nlm.nih.gov/29516039, https://www.ncbi.nlm.nih.gov/pmc/articles/PMC5836359/.

[32] B. Danielson, K. Frennered, G. Selvik, L. Irstam, Roentgenologic Assessment of Spondylolisthesis, Acta Radiol. 30 (1989) 65–68, https://doi.org/10.3109/02841858909177460.

[33] J.R. Dimar, L.Y. Carreon, H. Labelle, M. Djurasovic, M. Weidenbaum, C. Brown, P. Roussouly, Intra- and inter-observer reliability of determining radiographic sagittal parameters of the spine and pelvis using a manual and a computer-assisted methods, Eur. Spine J. 17 (2008), https://doi.org/10.1007/s00586-008-0755-1.

[34] T.J. Errico, B.S. Lonner, A.W. Moulton, Surgical Management of Spinal Deformities. Elsevier Inc., 2009. 10.1016/B978-1-4160-3372-1.X5001-X.

[35] K. Gelse, S. Söder, W. Eger, T. Diemtar, T. Aigner, Osteophyte development-molecular characterization of differentiation stages, Osteoarthritis Cartilage 11 (2003) 141–148, https://doi.org/10.1053/JOCA.2002.0873.

[36] S.D. Glassman, K. Bridwell, J.R. Dimar, W. Horton, S. Berven, F. Schwab, The impact of positive sagittal balance in adult spinal deformity, Spine (2005), https://doi.org/10.1097/01.brs.0000179086.30449.96.

[37] B. Glocker, Dataset — UWSpineCT. https://imperialcollegelondon.app.box.com/s/erhcm28aablpy1725lt93xh6pk31ply1.

[38] B. Glocker, J. Feulner, A. Criminisi, D.R. Haynor, E. Konukoglu, Automatic localization and identification of vertebrae in arbitrary field-of-view CT scans, 2012, pp. 590–598. DOI: 10.1007/978-3-642-33454-2_73.

[39] I.A. Harris, A. Traeger, R. Stanford, C.G. Maher, R. Buchbinder, Lumbar spine fusion: what is the evidence? Internal Med. J. 48 (2018) 1430–1434, https://doi.org/10.1111/imj.14120.

[40] D.D. Harrison, R. Cailliet, T.J. Janik, S.J. Troyanovich, D.E. Harrison, B. Holland, Elliptical modeling of the sagittal lumbar lordosis and segmental rotation angles as a method to discriminate between normal and low back pain subjects, J. Spinal Disorders 11 (1998) 430–439. URL: https://pubmed.ncbi.nlm.nih.gov/9811104/.

[41] D.E. Harrison, R. Cailliet, D.D. Harrison, T.J. Janik, B. Holland, Reliability of centroid, Cobb, and Harrison posterior tangent methods: which to choose for analysis of thoracic kyphosis, Technical Report 11 (2001), https://doi.org/10.1097/00007632-200106010-00002.

[42] D.E. Harrison, D.D. Harrison, R. Cailliet, S.J. Troyanovich, T.J. Janik, B. Holland, Cobb Method or Harrison Posterior Tangent Method, Spine 25 (2000) 2072–2078, https://doi.org/10.1097/00007632-200008150-00011.

[43] J. Hartman, M. Granville, R.E. Jacobson, Radiologic Evaluation Of Lumbar Spinal Stenosis: The Integration Of Sagittal And Axial Views In Decision Making For Minimally Invasive Surgical Procedures, Cureus (2019), https://doi.org/10.7759/cureus.4268.

[44] K. Hasegawa, M. Okamoto, S. Hatsushikano, H. Shimoda, M. Ono, K. Watanabe, Normative values of spino-pelvic sagittal alignment, balance, age, and health-related quality of life in a cohort of healthy adult subjects, Eur. Spine J. 25 (2016), https://doi.org/10.1007/s00586-016-4702-2.

[45] K. Hashimoto, T. Aizawa, H. Kanno, E. Itoi, Adjacent segment degeneration after fusion spinal surgery-a systematic review, Int. Orthop. 43 (2019), https://doi.org/10.1007/s00264-018-4241-z.
[46] T. Hassan, M.U. Akram, N. Werghi, Evaluation of deep segmentation models for the extraction of retinal lesions from multi-modal retinal images, 2020. arXiv:2006.02662.
[47] T. Hassan, M.U. Akram, N. Werghi, N. Nazir, RAG-FW: A hybrid convolutional framework for the automated extraction of retinal lesions and lesion-influenced grading of human retinal pathology, IEEE J. Biomed. Health Inf. (2020) 1, https://doi.org/10.1109/JBHI.2020.2982914.
[48] T. Hassan, N. Werghi, Exploiting the Transferability of Deep Learning Systems Across Multi-modal Retinal Scans for Extracting Retinopathy Lesions, in: 2020 IEEE 20th International Conference on Bioinformatics and Bioengineering (BIBE), IEEE, 2020, https://doi.org/10.1109/BIBE50027.2020.00099.
[49] K. He, X. Zhang, S. Ren, J. Sun, Deep residual learning for image recognition. CoRR abs/1512.03385, 2015. http://arxiv.org/abs/1512.03385, arXiv:1512.03385.
[50] A.G. Howard, M. Zhu, B. Chen, D. Kalenichenko, W. Wang, T. Weyand, M. Andreetto, H. Adam, MobileNets: Efficient Convolutional Neural Networks for Mobile Vision Applications, 2017 arXiv arXiv:1704.04861.
[51] B. Howe, A. Gururajan, H. Sari-Sarraf, L.R. Long, Hierarchical segmentation of cervical and lumbar vertebrae using a customized generalized hough transform and extensions to active appearance models, in: Proceedings of the IEEE Southwest Symposium on Image Analysis and Interpretation, 2004, pp. 182–186, https://doi.org/10.1109/iai.2004.1300970.
[52] J. Huang, H. Shen, J. Wu, X. Hu, Z. Zhu, X. Lv, Y. Liu, Y. Wang, Spine Explorer: a deep learning based fully automated program for efficient and reliable quantifications of the vertebrae and discs on sagittal lumbar spine MR images, Spine J. 20 (2020) 590–599, https://doi.org/10.1016/j.spinee.2019.11.010.
[53] A. Ishihara, Roentgenographic studies on the normal pattern of the cervical curvature, J. Japanese Orthopaedic Assoc. 42 (1968) 1033–1044.
[54] R. Janssens, G. Zheng, Deep Learning based Segmentation of Lumbar Vertebrae from CT Images, 2018. 10.29007/vt7v.
[55] J. Jing, Z. Wang, M. Rätsch, H. Zhang, Mobile-Unet: An efficient convolutional neural network for fabric defect detection, Text. Res. J. (2020), https://doi.org/10.1177/0040517520928604.
[56] C. JR, Outlline for the Study of Scoliosis. American Academy of Orthopaedic Surgeons 5 (1948) 261.
[57] G.U. Kim, M.C. Chang, T.U. Kim, G.W. Lee, Asian Spine Journal - pISSN 1976–1902 eISSN 1976–7846 - www.asianspinejournal.org Asian Spine. Asian Spine J. 14 (2020) 910–920. 10.31616/asj.2020.0593.
[58] J. Kim, S.J. Yang, H. Kim, Y. Kim, J.B. Park, C. DuBose, T.H. Lim, Effect of Shear Force on Intervertebral Disc (IVD) Degeneration: An In Vivo Rat Study, Ann. Biomed. Eng. 40 (2012) 1996–2004, https://doi.org/10.1007/s10439-012-0570-z.
[59] M.R. Konieczny, S. Schroer, C. Schleich, M. Prost, M. Hufeland, H. Kubo, R. Krauspe, Lumbar lordosis as tool to assess the level of pain in patients with low back pain after lumbar disc herniation, J. Orthopaedics 22 (2020) 190–193, https://doi.org/10.1016/j.jor.2020.04.010.
[60] M.A. Larhmam, S. Mahmoudi, M. Benjelloun, Semi-automatic detection of cervical vertebrae in X-ray images using generalized hough transform, in: 2012 3rd International Conference on Image Processing Theory, Tools and Applications (IPTA), IEEE, 2012, https://doi.org/10.1109/IPTA.2012.6469570.
[61] N. Lessmann, B. van Ginneken, P.A. de Jong, I. Išgum, Iterative fully convolutional neural networks for automatic vertebra segmentation and identification, Med. Image Anal. 53 (2019) 142–155, https://doi.org/10.1016/j.media.2019.02.005, arXiv:1804.04383.
[62] G. Litjens, T. Kooi, B.E. Bejnordi, A.A.A. Setio, F. Ciompi, M. Ghafoorian, J.A. van der Laak, B. van Ginneken, C.I. Sánchez, A survey on deep learning in medical image analysis, 2017. 10.1016/j.media.2017.07.005, arXiv:1702.05747.
[63] X. Liu, Y. Zhang, H. Jing, L. Wang, S. Zhao, Ore image segmentation method using U-Net and Res_Unet convolutional networks, RSC Adv. 10 (2020) 9396–9406, https://doi.org/10.1039/c9ra05877j.
[64] Lloyd-Jones Graham, 2017. MRI interpretation - T1 v T2 images. https://www.radiologymasterclass.co.uk/tutorials/mri/t1_and_t2_images.
[65] M.T. Löffler, A. Sekuboyina, A. Jacob, A.L. Grau, A. Scharr, M. El Husseini, M. Kallweit, C. Zimmer, T. Baum, J.S. Kirschke, A Vertebral Segmentation Dataset with Fracture Grading, Radiol.: Artif. Intell. 2 (2020), e190138, https://doi.org/10.1148/ryai.2020190138.
[66] G. Logroscino, W. Lattanzi, Bone Substitution in Spine Fusion: The Past, the Present, and the Future, in: Minimally Invasive Surgery of the Lumbar Spine. Springer, London, London, 2014. DOI: 10.1007/978-1-4471-5280-4_15.
[67] J. Long, E. Shelhamer, T. Darrell, Fully convolutional networks for semantic segmentation, in: 2015 IEEE Conference on Computer Vision and Pattern Recognition (CVPR), IEEE, 2015, pp. 3431–3440, https://doi.org/10.1109/CVPR.2015.7298965.
[68] J.T. Lu, S. Pedemonte, B. Bizzo, S. Doyle, K.P. Andriole, M.H. Michalski, R.G. Gonzalez, S.R. Pomerantz, DeepSPINE: Automated Lumbar Vertebral Segmentation, Disc-level Designation, and Spinal Stenosis Grading Using Deep Learning, 2018. arXiv 85, 1–16. arXiv:1807.10215.
[69] K. Luoma, H. Riihimäki, R. Luukkonen, R. Raininko, E. Viikari-Juntura, A. Lamminen, Low back pain in relation to lumbar disc degeneration, Spine (2000), https://doi.org/10.1097/00007632-200002150-00016.
[70] N.J. MacIntyre, L. Bennett, A.M. Bonnyman, P.W. Stratford, Optimizing Reliability of Digital Inclinometer and Flexicurve Ruler Measures of Spine Curvatures in Postmenopausal Women with Osteoporosis of the Spine: An Illustration of the Use of Generalizability Theory, ISRN Rheumatol. 2011 (2011), https://doi.org/10.5402/2011/571698.
[71] N.J. MacIntyre, C.P. Recknor, J.C. Recknor, Spine Curve Measures Taken in Individuals with Osteoporosis and Osteopenia Using the IONmed Mobile Phone Application Are Highly Consistent with Digital Inclinometer Measures, ISRN Rehab. 2014 (2014), https://doi.org/10.1155/2014/508414.
[72] Mark, How to fix sway back posture. http://posturedirect.com/how-to-fix-sway-back-posture/.
[73] I.S. Masad, A. Al-Fahoum, I. Abu-Qasmieh, Automated measurements of lumbar lordosis in T2-MR images using decision tree classifier and morphological image processing, Eng. Sci. Technol. 22 (2019) 1027–1034, https://doi.org/10.1016/j.jestch.2019.03.002.
[74] MATLAB, 2020. 9.8.0.1323502 (R2020a). The MathWorks Inc., Natick, Massachusetts.
[75] W. Mbarki, M. Bouchouicha, S. Frizzi, F. Tshibasu, L.B. Farhat, M. Sayadi, Lumbar spine discs classification based on deep convolutional neural networks using axial view MRI, Interdiscip. Neurosurg.: Adv. Tech. Case Manage. 22 (2020), https://doi.org/10.1016/j.inat.2020.100837.
[76] Medixant, Radiant dicom viewer. https://www.radiantviewer.com.
[77] Mehmet Demir, E. Gumusburun, N. Seringec, M. Cicek, R. Ertugrul, Bulent Guneri Department of Orthopedics and Traumatology, Faculty of Medicine, Kahramanmaras Sutcu Imam University, K., Radiographic analysis of the lumbar and sacral region angles in young Turkish adults. J. Pakistan Med. Assoc. 68 (2018). 10.3109/17453678409153740.
[78] A. Mehmood, M. Usman Akram, M. Akhtar, Vertebra Localization using Shape based analysis and unsupervised Clustering from X-Ray Images, PJCIS 1 (2016) 13–24, http://173.208.131.244:9060/xmlui/handle/123456789/823.
[79] J.L. Melancia, A.F. Francisco, J.L. Antunes, Spinal stenosis, in: Handbook of Clinical Neurology. Elsevier B.V. vol. 119, 2014, pp. 541–549. DOI: 10.1016/B978-0-7020-4086-3.00035-7.
[80] H.W. Meyerding, Spondyloptosis, Surg. Gynaecol. Obstet. 54 (1932) 371–377.
[81] F. Monteiro, A.C. Campilho, Distance measures for image segmentation evaluation, AIP Conf. Proc. (2012) 794–797, https://doi.org/10.1063/1.4756257.
[82] F.C. Monteiro, A.C. Campilho, Performance evaluation of image segmentation, International Conference Image Analysis and Recognition, Springer (2006) 248–259, http://link.springer.com/10.1007/11867586_24.
[83] D. Moore, Spine Biomechanics – Spine – Orthobullets, 2019. https://www.orthobullets.com/spine/2003/spine-biomechanics.
[84] A.L. Nachemson, Acta Orthopaedica Scandinavica Evaluation of results in lumbar spine surgery, 2009. https://www.tandfonline.com/action/journalInformation?journalCode=iort20, DOI: 10.3109/17453679309160143.
[85] F. Natalia, H. Meidia, N. Afriliana, A.S. Al-Kafri, S. Sudirman, A. Simpson, A. Sophian, M. Al-Jumaily, W. Al-Rashdan, M. Bashtawi, Development of Ground Truth Data for Automatic Lumbar Spine MRI Image Segmentation, in: Proceedings – 20th International Conference on High Performance Computing and Communications, 16th International Conference on Smart City and 4th International Conference on Data Science and Systems, HPCC/SmartCity/DSS 2018, 2019, pp. 1449–1454. DOI: 10.1109/HPCC/SmartCity/DSS.2018.00239.
[86] F.O. Okpala, Comparison of four radiographic angular measures of lumbar lordosis, J. Neurosci. Rural Practice 9 (2018) 298–304, https://doi.org/10.4103/jnrp.jnrp_508_17.
[87] T.S. de Oliveira, C.T. Candotti, M. La Torre, P.P.T. Pelinson, T.S. Furlanetto, F. M. Kutchak, J.F. Loss, Validity and Reproducibility of the Measurements Obtained Using the Flexicurve Instrument to Evaluate the Angles of Thoracic and Lumbar Curvatures of the Spine in the Sagittal Plane, Rehab. Res. Practice 2012 (2012), https://doi.org/10.1155/2012/186156.
[88] OSF, 2019. OSF — VerSe2019. https://osf.io/nqjyw/.
[89] S. Pang, Z. Su, S. Leung, I.B. Nachum, B. Chen, Q. Feng, S. Li, Direct automated quantitative measurement of spine by cascade amplifier regression network with manifold regularization, Med. Image Anal. 55 (2019) 103–115, https://doi.org/10.1016/j.media.2019.04.012.
[90] Peter Ullrich, Lumbar Spine Surgery. https://www.spine-health.com/treatment/back-surgery/lumbar-spine-surgery.
[91] Physiopedia, Low Back Pain Related to Hyperlordosis – Physiopedia. https://www.physio-pedia.com/index.php?title=Low_Back_Painl726 Related_to_Hyperlordosis&oldid=234487.
[92] D.W. Polly, F.X. Kilkelly, K.A. McHale, L.M. Asplund, M. Mulligan, A.S. Chang, Measurement of Lumbar Lordosis. Evaluation of intraobserver, interobserver, and technique variability, Spine 21 (1996) 1530–1535, https://doi.org/10.1097/00007632-199607010-00008.
[93] F. Raciborski, R. Gasik, A. Kłak, Disorders of the spine. a major health and social problem, Reumatologia 54 (2016) 196. URL: https://www.ncbi.nlm.nih.gov/pmc/articles/PMC5090028/.
[94] P.P. Raj, Intervertebral disc: Anatomy-physiology-pathophysiology-treatment, 2008. 10.1111/j.1533-2500.2007.00171.x.
[95] P. Rajnics, V. Pomero, A. Templier, F. Lavaste, T. Illes, Computer-Assisted Assessment of Spinal Sagittal Plane Radiographs, J. Spinal Disord. 14 (2001), https://doi.org/10.1097/00002517-200104000-00008.
[96] M. Rak, J. Steffen, A. Meyer, C. Hansen, K.D. Tönnies, Combining convolutional neural networks and star convex cuts for fast whole spine vertebra segmentation in MRI, Comput. Methods Programs Biomed. 177 (2019) 47–56, https://doi.org/10.1016/j.cmpb.2019.05.003.
[97] J. Roland, Lower Back Spasms: Causes, Diagnosis, and Treatment. https://www.healthline.com/health/back-pain/lower-back-spasms#causes.

[98] O. Ronneberger, P. Fischer, T. Brox, U-net: Convolutional networks for biomedical image segmentation, in: Lecture Notes in Computer Science (including subseries Lecture Notes in Artificial Intelligence and Lecture Notes in Bioinformatics), Springer Verlag, 2015, pp. 234–241. DOI: 10.1007/978-3-319-24574-4_28, arXiv:1505.04597.
[99] R.J. Rothrock, I.T. McNeill, K. Yaeger, E.K. Oermann, S.K. Cho, J.M. Caridi, Lumbar Lordosis Correction with Interbody Fusion: Systematic Literature Review and Analysis, 2018. 10.1016/j.wneu.2018.06.216.
[100] B. Roudsari, J.G. Jarvik, Lumbar spine MRI for low back pain: Indications and yield, 2010. 10.2214/AJR.10.4367.
[101] P. Roussouly, S. Gollogly, E. Berthonnaud, J. Dimnet, Classification of the Normal Variation in the Sagittal Alignment of the Human Lumbar Spine and Pelvis in the Standing Position, Spine 30 (2005), https://doi.org/10.1097/01.brs.0000152379.54463.65.
[102] S.H. Roy, C.J. De Luca, D.A. Casavant, Lumbar muscle fatigue and chronic lower back pain, Spine 14 (1989) 992–1001. URL: https://pubmed.ncbi.nlm.nih.gov/2528828/.
[103] B.S. Russell, K.A. Muhlenkamp, K.T. Hoiriis, C.M. DeSimone, Measurement of lumbar lordosis in static standing posture with and without high-heeled shoes, J. Chiropractic Med. 11 (2012) 145–153, https://doi.org/10.1016/j.jcm.2012.02.002.
[104] B.S. Russell, K.A. Muhlenkamp-Wermert, K.T. Hoiriis, Measurement of Lumbar Lordosis: A Comparison of 2 Alternatives to the Cobb Angle, J. Manipulative Physiol. Ther. (2020), https://doi.org/10.1016/j.jmpt.2020.05.009.
[105] H. Saraste, Spondylolysis and spondylolisthesis, Acta Orthop. Scand. 64 (1993) 84–86, https://doi.org/10.3109/17453679309160129. URL: https://orthoinfo.aaos.org/en/diseases-conditions/spondylolysis-and-spondylolisthesis.
[106] N. Saxena, K.B. N, B. Raman, Semantic Segmentation of Multispectral Images using Res-Seg-net Model, in: 2020 IEEE 14th International Conference on Semantic Computing (ICSC), 2020, pp. 154–157. 10.1109/ICSC.2020.00030.
[107] M.I. Sezan, A.M. Tekalp, R. Schaetzing, Automatic Anatomically Selective Image Enhancement in Digital Chest Radiography, IEEE Trans. Med. Imaging 10 (1109/42) (1989) 24863.
[108] H. Shemshaki, M. Etemadifar, M. Fereidan-Esfahani, M. Mokhtari, S.M. Nourian, What is the source of low back pain? J. Craniovertebral Junction Spine 4 (2013) https://doi.org/10.4103/0974-8237.121620.
[109] Y. Shen, V.S. Sheng, L. Wang, J. Duan, X. Xi, D. Zhang, Z. Cui, Empirical comparisons of deep learning networks on liver segmentation. Comput. Mater. Continua 62 (2020) 1233–1247. 10.32604/cmc.2020.07450.
[110] P. Smyth, C. Taylor, J. Adams, Automatic measurement of vertebral shape using active shape models, Image Vis. Comput. 15 (1997), https://doi.org/10.1016/S0262-8856(97)00006-1.
[111] P. Soille, P. Soille, Opening and Closing, in: Morphological Image Analysis. Springer, Berlin Heidelberg, Berlin, Heidelberg, 1999, pp. 89–127. DOI: 10.1007/978-3-662-03939-7_4.
[112] SpineWeb.
[113] I.A.F. Stokes, Three-dimensional terminology of spinal deformity. A report presented to the Scoliosis Research Society by the Scoliosis Research Society Working Group on 3-D terminology of spinal deformity. Spine (1994). 10.1097/00007632-199401001-00020.
[114] S. Sudirman, A. Al Kafri, F. Natalia, H. Meidia, N. Afriliana, W. Al-Rashdan, M. Bashtawi, M. Al-Jumaily, Lumbar Spine MRI Dataset, Mendeley Data 2 (2019). URL: https://data.mendeley.com/datasets/k57fr854j2/2.
[115] P. Suri, E.J. Boyko, J. Goldberg, C.W. Forsberg, J.G. Jarvik, Longitudinal associations between incident lumbar spine MRI findings and chronic low back pain or radicular symptoms: retrospective analysis of data from the longitudinal assessment of imaging and disability of the back (LAIDBACK), BMC Musculoskeletal Disorders 15 (2014) 152, https://doi.org/10.1186/1471-2474-15-152.
[116] A. Suzani, A. Seitel, Y. Liu, S.S. Fels, R.N. Rohling, P. Abolmaesumi, Fast automatic vertebrae detection and localization in pathological CT scans – A deep learning approach, in: Navab, N., Hornegger, J., III, W.M.W., Frangi, A.F. (Eds.), Medical Image Computing and Computer-Assisted Intervention - MICCAI 2015–18th International Conference Munich, Germany, October 5–9, 2015, Proceedings, Part III, Springer, 2015, pp. 678–686. DOI: 10.1007/978-3-319-24574-4_81.
[117] A.A. Taha, A. Hanbury, Evaluation Metrics for Medical Organ Segmentation and Lesion Detection, in: Cloud-Based Benchmarking of Medical Image Analysis. Springer International Publishing, 2017, pp. 87–105. DOI: 10.1007/978-3-319-49644-3_6.
[118] H. Tang, X. Pei, S. Huang, X. Li, C. Liu, Automatic Lumbar Spinal CT Image Segmentation with a Dual Densely Connected U-Net, IEEE Access 8 (2020) 89228–89238, https://doi.org/10.1109/ACCESS.2020.2993867, arXiv:1910.09198.
[119] Y. Tao, Z. Ling, I. Patras, Universal Foreground Segmentation Based on Deep Feature Fusion Network for Multi-Scene Videos. IEEE Access (2019) 1. DOI: 10.1109/ACCESS.2019.2950639.
[120] G. Van Rossum, F.L. Drake, Python 3 Reference Manual, CreateSpace, Scotts Valley, CA, 2009.
[121] R. Vialle, N. Levassor, L. Rillardon, A. Templier, W. Skalli, P. Guigui, Radiographic Analysis of the Sagittal Alignment and Balance of the Spine in Asymptomatic Subjects, J. Bone Joint Surg. 87 (2005), https://doi.org/10.2106/JBJS.D.02043.
[122] S.A. Voutsinas, G.D. MacEwen, Sagittal Profiles of the Spine. Clinical Orthopaedics and Related Research 210, 1986. URL: https://journals.lww.com/clinorthop/Fulltext/1986/09000/Sagittal_Profiles_of_the_Spine.34.aspx.
[123] T. Vrtovec, B. Likar, F. Pernuš, Manual and computerized measurement of sagittal vertebral inclination in computed tomography images, Spine 36 (2011), https://doi.org/10.1097/BRS.0b013e3181fe0aab.
[124] T. Vrtovec, F. Pernuš, B. Likar, A review of methods for quantitative evaluation of spinal curvature, Eur. Spine J. 18 (2009) 593–607, https://doi.org/10.1007/s00586-009-0913-0.
[125] L. Wang, Q. Xu, S. Leung, J. Chung, B. Chen, S. Li, Accurate automated Cobb angles estimation using multi-view extrapolation net, Med. Image Anal. 58 (2019), 101542, https://doi.org/10.1016/j.media.2019.101542.
[126] B.P. Yang, C.W. Yang, S.L. Ondra, A novel mathematical model of the sagittal spine, Spine 32 (2007) 466–470, https://doi.org/10.1097/01.brs.0000255207.44141.e9.
[127] G. Zanoli, B. Jönsson, B. Strömqvist, Acta Orthopaedica SF-36 scores in degenerative lumbar spine disorders: Analysis of prospective data from 451 patients SF-36 scores in degenerative lumbar spine disorders Analysis of prospective data from 451 patients, Acta Orthopaedica 77 (2006) 298–306, https://doi.org/10.1080/17453670610046064, https://www.tandfonline.com/action/journalInformation?journalCode=iort20.
[128] M.D. Zeiler, ADADELTA: an adaptive learning rate method. CoRR abs/1212.5701, 2012. http://arxiv.org/abs/1212.5701, arXiv:1212.5701.
[129] J. Zhang, H. Li, L. Lv, Y. Zhang, Computer-Aided Cobb Measurement Based on Automatic Detection of Vertebral Slopes Using Deep Neural Network, Int. J. Biomed. Imaging 2017 (2017), https://doi.org/10.1155/2017/9083916.
[130] R. Zhang, L. Du, Q. Xiao, J. Liu, Comparison of Backbones for Semantic Segmentation Network, J. Phys: Conf. Ser. 1544 (2020), https://doi.org/10.1088/1742-6596/1544/1/012196.
[131] Y.J. Zhang, A review of recent evaluation methods for image segmentation, in: 6th International Symposium on Signal Processing and Its Applications, ISSPA 2001 – Proceedings; 6 Tutorials in Communications, Image Processing and Signal Analysis, 2001, pp. 148–151. DOI: 10.1109/ISSPA.2001.949797.
[132] H. Zhao, J. Shi, X. Qi, X. Wang, J. Jia, Pyramid Scene Parsing Network, in: 2017 IEEE Conference on Computer Vision and Pattern Recognition (CVPR), IEEE, 2017, pp. 6230–6239. DOI: 10.1109/CVPR.2017.660, arXiv:1612.01105.
[133] Z. Zhou, M.M.R. Siddiquee, N. Tajbakhsh, J. Liang, Unet++: Redesigning skip connections to exploit multiscale features in image segmentation, IEEE Trans. Medical Imaging 39 (2020) 1856–1867, https://doi.org/10.1109/TMI.2019.2959609.
[134] X. Zhu, X. He, P. Wang, Q. He, D. Gao, J. Cheng, B. Wu, A method of localization and segmentation of intervertebral discs in spine MRI based on Gabor filter bank, BioMed. Eng. OnLine 15 (2016) 32, https://doi.org/10.1186/s12938-016-0146-5.
[135] K. Zuiderveld, Contrast Limited Adaptive Histogram Equalization, in: Graphics Gems, 1994. DOI: 10.1016/b978-0-12-336156-1.50061-6.